Advanced Materials, Radiation Physics, and Intelligent Engineering Applications

Editor
ABDULLAH GÖKTAŞ

BİDGE

BİDGE Yayınları

Advanced Materials, Radiation Physics, and Intelligent Engineering Applications

Editor: ABDULLAH GÖKTAŞ

ISBN: 978-625-8567-99-1

1st Edition
Page Layout By: Gözde YÜCEL
Publication Date: 2025-12-25
BİDGE Yayınları

Certificate No: 71374

www.bidgeyayinlari.com.tr - bidgeyayinlari@gmail.com
Krc Bilişim Ticaret ve Organizasyon Ltd. Şti.
Güzeltepe Mahallesi Abidin Daver Sokak Sefer Apartmanı No: 7/9 Çankaya / Ankara

İÇİNDEKİLER

CHAPTER 1

THEORETİCAL STUDY OF X-RAYS AND COSTER–KRONİG ENHANCEMENT FACTORS İN THE L-SUBSHELL OF Sm, Eu, AND Bi ELEMENT

Rafet YILMAZ[1]
Abdullah ÖZKARTAL[2]

INTRODUCTION

The excitation of an atom, particularly its inner shell electrons, can lead to various processes. Photoionization induces the ejection of an inner shell electron, creating a vacancy. This vacancy can be filled by another electron, producing L X-ray emission characterized by the L XRF yield. Alternatively, the released energy can be imparted to another electron, resulting in the emission of an Auger electron, characterized by the Auger yield. In addition, CK transitions between subshells of the same shell play a significant role in the rearrangement of atomic energy levels and influence both X-ray emission and Auger

[1] Prof. Dr. Van Yüzüncü Yıl University Department of Physics, Faculty of Science, Orcıd: 000-0003-2734-8763
[2] Assoc. Prof. Dr. Van Yüzüncü Yıl University Department of Physics, Faculty of Science,, Orcıd: 0000-0002-1556-6141

processes. These parameters provide fundamental data for understanding atomic interactions and X-ray spectroscopy. Coster-Kronig transitions are defined as non-radiating de-excitation processes occurring between subshells within the same main shell. Atomic inner shell processes play a fundamental role in understanding the excitation and de-excitation mechanisms of atoms. A vacancy in an atom's inner shell makes the atom energetically unstable, and the system transitions to a less energetic state through various radiative or non-radiative transition mechanisms to fill this void. In this context, C-K transitions, which hold an important place among non-radiative transitions, are considered a special subclass of Auger processes. Coster-Kronig transitions were first described by Dirk Coster and Ralph Kronig (1935). These transitions can be thought of as follows: For example, a void in the L_1 subshell can be replenished by an electron from the L_2 or L_3 subshell, and the released energy can cause another electron from the same main shell to be ejected from the atom. This property distinguishes Coster-Kronig transitions from classical Auger transitions that occur between main shells. Due to relatively small energy differences, Coster-Kronig transitions are energetically possible only within specific atomic number ranges and for specific subshell combinations. The probability of these transitions depends heavily on factors such as subshell binding energies, atomic number, and electron-electron interactions. The probability of Coster-Kronig processes increases significantly for L and M shells, especially in medium and heavy elements. The presence of Coster-Kronig transitions significantly influences atomic de-excitation processes and

plays a decisive role in fluorescence yields, Auger electron energies, and spectral line densities. Therefore, accurate accounting of C-K transitions is necessary in many experimental and theoretical studies such as XRF spectroscopy, Auger electron spectroscopy (AES), and atomic shell modeling.

Estimating XRF cross-sections is challenging, especially for L_3 subshell lines, due to Coster–Kronig transitions. Transitions from the L_1 and L_2 subshells enhance the L_3 population, leading to increased Lα and related fluorescence cross-sections.

Consequently, C-K transitions are a fundamental process in atomic structure physics and are critical for understanding the de-excitation dynamics of inner shell vacancies. Detailed study of these transitions is indispensable for both fundamental atomic physics and applied spectroscopic techniques.

Many researchers have been conducted on the photoionization cross sections, fluorescence yields, Auger effect, C-K transitions, and intensification factors of *L* X-rays that may occur in the L shell of various elements. Hubbell et al. (1994) comprehensively investigated the X-ray fluorescence yields of the *K, L*, and higher shells of elements, compiled the relevant literature, and presented the data in tabular form, providing a reference source for X-ray fluorescence analyses and atomic parameter calculations. Krause et al. (1978) reported *K*- and *L*-shell XRF cross sections for many elements, derived from fundamental atomic parameters including photoionization cross sections, *W*, and transition probabilities, and

presented the results in tabulated form. This report serves as a standard reference in XRF analyses and atomic parameter studies. Scofield (1972) calculated theoretical photoionization cross sections for photons at 1–1500 keV. The study determined photoionization probabilities for the inner shells of different elements using theoretical models, and the results were compiled for use in scientific calculations and X-ray analyses. This work is regarded as a fundamental reference for atomic interaction parameters and X-ray spectroscopy. Scofield (1976) calculated subshell photoionization cross sections of various elements at 1254 and 1487 eV using the Hartree-Slater model, providing essential theoretical photoionization data for electron spectroscopy and X-ray analyses. Ertuğrul (2002) experimentally measured the L-subshell production cross sections and C-K (f_{12}) transition probabilities for Hg (Mercury) and Au (Gold) at a photon energy of 59.5 keV. This work provides important data for *L* X-ray spectral analyses and understanding Coster–Kronig transitions. Miranda et al. (2004) studied the influence of multiple ionization on L-shell X-ray production cross sections induced by proton impact. The study experimentally investigated the effect of multiple ionization induced by proton collisions on L X-ray production cross sections and discussed the obtained results. Other significant studies in this field include: Ertuğrul, 2002; Kaya and Ertuğrul, 2003; Onho, 2001; Söğüt et al., 2002; Barrea et al., 2004; Unterumsberger et al.,2018; Bonziet al.,2006; Meddouh et al.,2023; Chauhanet al.,2008;Menesquenet al.,2020; nica et al, 2005; Raulo et al.,2007; Sahnoune et al., 2020;Turhan et al.,2007)

Öz et al. (2001) experimentally measured the *L*-shell Coster-Kronig transition yields for several elements with atomic numbers 59 ≤ Z ≤ 90. The study provides important experimental data for understanding *L*-shell electron transitions and Coster–Kronig processes. Öz, et al., (2004) experimentally measured the Coster–Kronig enhancement factors for several elements with atomic numbers 74 ≤ Z ≤ 90. The work provides important data for the quantitative understanding of *L*-shell electron transitions and Coster–Kronig processes. New studies exist within the K-shell. In the study by Manoj and Sripathi Punchithaya (2025), the K-shell fluorescence parameters of low atomic number transition elements were experimentally determined using excitation with Au–Lα X-rays. K_α and K_β X-ray cross-sections and fluorescence yields were calculated.

In this study, the *L*-X-ray photoionization cross-sections and C-K transition intensification factors of the *L*-sublayers of Sm (Samarium), Eu (Europyum) and Bi (Bismuth) elements were theoretically calculated. Three cases were examined in study to investigate the role of C-K transitions on the increase in *L*-XRF cross-sections and *L*-X-ray intensity. These conditions require the excitation energy to be higher than the binding energies of the L subshells, but not sufficient to excite another subshell. Therefore, three distinct cases arise due to the presence of three subshells. In these studies, both theoretical and experimental, the energy and element that correspond to the secondary source energy needed to excite each subshell are identified.

Fluorescence Yield, Coster-Kronig Transitions and Auger Process

The fluorescence yield defined for a specific shell or subshell of an atom represents the probability that a vacancy in that shell, resulting from any interaction, will be filled by characteristic X-ray emission. When an electron vacancy is created in an atom, the atom enters an excited state. If the average lifetime of this excited state is denoted by τ, then, according to the energy-time uncertainty principle, the total level width of this state is defined as $\Gamma = \hbar/\tau$. The total level width Γ is expressed as the sum of the contributions Γ_R (corresponding to radiative transitions), Γ_A (corresponding to non-radiative (Auger) transitions), and Γ_{CK} (resulting from Coster–Kronig processes). The totol level width toplam seviye genişliği ($\Gamma = \Gamma_R + \Gamma_A + \Gamma_{CK}$) (Jenkins,1986). Therefore, fluorescence efficiency,

$$\omega = \frac{\Gamma_R}{\Gamma} \qquad (1)$$

It is given with.

The probability that a void created in the K shell of an atom is filled through the emission of characteristic X-rays is defined as the K-shell *w*

$$\omega_K = \frac{I_K}{n_K} \qquad (2)$$

It is given by the relationship. Here, I_K the number of X-rays emitted from the sample is K, where n_K is the number of void created in the K layer. For higher atomic layers, the definition of fluorescence efficiency is more complex for two reasons: Alt tabakalara sahip tabakalarda C-K geçişleri söz konusudur. Bu geçişler, aynı baş kuantum sayısına sahip alt tabakalar arasında elektron veya boşluk kaymalarına neden olur. Different ionization models give rise to different vacancy distributions in atomic shells and subshells. Consequently, the average fluorescence yield depends strongly on the specific ionization mechanism by which these shells are excited. C-K transitions can occur in atomic shells that are divided into subshells. These transitions represent the redistribution of electrons or vacancies among subshells. The probability of a C-K transition is denoted by $f_{ij.}$

In atoms, an electron vacancy can be occupied by electrons from higher energy levels. This filling process can occur through two distinct mechanisms: radiative or non-radiative. One of the non-radiative processes, known as the Auger effect, occurs when an electron from an upper energy level fills the void, causing another electron to be emitted from the atom. As a result, the atom reaches a doubly excited state. The electron ejected during the Auger process is referred to as an Auger electron. Such processes are commonly termed non-radiative transitions or Auger transitions in the literature.

Theoretical *L* XRF Cross-sections

The L_ι L_α, L_β and $L\gamma$ play a crucial role in establishing reliable theoretical models in fundamental nuclear and atomic physics studies,

which describe the emission of X-rays and Auger electrons. These parameters can be theoretically calculated using subshell photoionization cross sections, *W*, C-K transition probabilities, and transition rates. In this context, the following relationships proposed by Mann et al.(1994) form the basis of these calculations. Theoretically, in the absence of Coster-Kronig enhancement (*fij*=0), the characteristic *L* X-ray sections are expressed as follows.

$$\sigma_{Ll} = \sigma_3 \omega_3 F_{3l} \tag{3}$$

$$\sigma_{L\alpha} = \sigma_3 \omega_3 F_{3\alpha} \tag{4}$$

$$\sigma_{L\beta} = \sigma_1 \omega_1 F_{1\beta} + \sigma_2 \omega_2 F_{2\beta} + \sigma_3 \omega_3 F_{3\beta} \tag{5}$$

$$\sigma_{L\gamma} = \sigma_1 \omega_1 F_{1\gamma} + \sigma_2 \omega_2 F_{2\gamma} \tag{6}$$

But in reality, C-K exist, and in this case, the cross-sections.

$$\sigma_{Ll} = [\sigma_1 (f_{13} + f_{12} f_{23}) + \sigma_2 f_{23} + \sigma_3] \omega_3 F_{3l} \tag{7}$$

$$\sigma_{L\alpha} = [\sigma_1 (f_{13} + f_{12} f_{23}) + \sigma_2 f_{23} + \sigma_3] \omega_3 F_{3\alpha} \tag{8}$$

$$\sigma_{L\beta} = \sigma_1 \omega_1 F_{1\beta} + (\sigma_1 f_{12} + \sigma_2) \omega_2 F_{2\beta} + [\sigma_3 + \sigma_2 f_{23} + \sigma_1 (f_{13} + f_{12} f_{23})] \omega_3 F_{3\beta} \tag{9}$$

$$\sigma_{L\gamma} = \sigma_1 \omega_1 F_{1\gamma} + (\sigma_1 f_{12} + \sigma_2) \omega_2 F_{2\gamma} \tag{10}$$

Here , σ are the fotoiyonizasyon cross-sections of the substrates and are calculated using the equation $\ln\sigma = k\,\mathrm{lnE}$ with the help of Scofield's table (1973). *f* are the C-K transition probabilities. ω, are the *W* of the substrates and are taken from Krause's tables (1979). *F* are the transmission rate probabilities for *L*-X-rays and are obtained from Scofield's tables (1969). In this study, L_l L_α, L_β was calculated theoretically.

The C-K enhancement factors are obtained by dividing the relevant equations side by side, taking into account the same X-rays (Öz etal.,2004). This approach allows for the quantitative determination of these factors and makes them an important parameter in fluorescence calculations.

$$\kappa_{l,\alpha} = \frac{\sigma_1(\, f_{13} + f_{12} f_{23}\,) + \sigma_2 f_{23} + \sigma_3}{\sigma_3} \qquad (11)$$

$$\kappa_\beta = \frac{\sigma_1\omega_1 F_{1\beta} + (\sigma_1 f_{12} + \sigma_2)\omega_2 F_{2\beta} + [\sigma_3 + \sigma_2 f_{23} + \sigma_1(\, f_{13} + f_{12} f_{23}\,)]\omega_3 F_{3\beta}}{\sigma_1\omega_1 F_{1\beta} + \sigma_2\omega_2 F_{2\beta} + \sigma_3\omega_3 F_{3\beta}} \qquad (12)$$

They are calculated using equations. When a vacancy occurs in the L_1 subshell, f_{12} and f_{23} type Coster–Kronig transitions can take place. In the L_2 subshell, only the f_{23} transition is possible. No Coster-Kronig transitions are observed in the L_3 subshell. The excitation energies of the elements are given in Table 1 (Elam, 2002).

***Table 1**. Absorption edge and excitation energies of Sm, Eu, and Bi elements*

Element	Absorption edge energy (keV)			Excitation energy (keV)		
	L_1	L_2	L_3	L_1	L_2	L_3
Sm	7.754	7.281	6.721	11.372	7.649	7.057
Eu	8.069	7.624	6.983	11.372	7.649	7.057
Bi	16.393	15.716	13.424	16.896	15.859	13.596

RESULTS AND DISCUSSION

The XRF of the *L* sublayers of Sm, Eu, and Bi elements were calculated using Equations 7, 8, and 9. The obtained values are presented in Tables 2-4.

An examination of Table 2-4 shows that the analysis of *L*-shell X-ray photoionization cross sections indicates that when elements are excited with energies below the L_1 subshell threshold, the photoionization cross sections associated with the excitation of the L_2 and L_3 subshells exhibit higher values. This trend can be explained by the dominance of the photoelectric effect at lower energies, which makes photoionization more probable for the L_2 and L_3 subshells within this energy range.

Table 2. $\sigma_{L\alpha}, \sigma_{L\beta}, \sigma_{Ll}$ *(barns-atom) (for* L_3*))*

Elemennt	**E (keV)**	$\sigma_{L\alpha}$	$\sigma_{L\beta}$	σ_{Ll}
Sm	7.057	6904.225	2190.813	277.852
Eu	7.057	7691.908	1371.207	309.930
Bi	13.596	8802.232	2069.516	477.580

Table 3. $\sigma_{L\alpha}, \sigma_{L\beta}, \sigma_{Ll}$ *(barns-atom)* (*for*L_2)

Elemennt	**E (keV)**	$\sigma_{L\alpha}$	$\sigma_{L\beta}$	σ_{Ll}
Sm	7.649	6104.328	4419.191	245.782
Eu	7.649	6802.788	4913.734	274.105
Bi	15.859	6206.639	5321.732	336.794

Table 4. $\sigma_{L\alpha}, \sigma_{L\beta}, \sigma_{Ll}$ *(barns-atom)* (for L_1)

Elemennt	**E (keV)**	$\sigma_{L\alpha}$	$\sigma_{L\beta}$	σ_{Ll}
Sm	11.372	2304.938	2190.813	92.759
Eu	11.372	2594.415	2461.757	104.536
Bi	16.896	6335.181	5584.750	343.769

As shown in Tables 2-4, the excitation energies for each element were selected by considering the absorption edge energies of the corresponding subshells. These energy choices were made to ensure consistency with the photoionization cross-sections calculated by Scofield. Since Sm and Eu have similar atomic numbers and the experimentally used excitation energies are within suitable ranges for both elements, the same excitation energies were adopted for these two elements. However, despite having the same excitation energies, it is clearly observed that the photoionization cross-sections of *L* X-rays increase with atomic number. In other words, as the atomic number increases, the photoionization cross-sections of X-rays also increase.

The findings obtained in this study clearly demonstrate that non-radiative transitions particularly C-K transitionshave a significant effect on the intensities of characteristic *L*-shell X-rays. C-K transitions cause vacancies created in the upper *L* subshells (L_1 and L_2) to be rapidly transferred to the L_3 subshell, thereby increasing the probability of characteristic X-ray emission originating from the L_3 subshell. This mechanism constitutes the fundamental physical reason for the observed increases in the measured X-ray intensities.

Table 5. *$K_{\alpha 1}$ and $K_{\alpha 2}$ C-K enhancement factors*

Elemennt	**E (keV)**	**K_{l1}**	**E (keV)**	**K_{l2}**
Sm	7.649	1.088	11.372	1.257
Eu	7.649	1.085	11.372	1.250
Bi	15.859	1.075	16.896	1.304

Table 6. *K_{l1} and K_{l2} C-K factors*

Elemennt	**E (keV)**	**$K_{\alpha 1}$**	**E (keV)**	**$K_{\alpha 2}$**
Sm	7.649	1.088	11.372	1.257
Eu	7.649	1.085	11.372	1.250
Bi	15.859	1.075	16.896	1.304

Table 7. *$K_{\beta 1}$ and $K_{\beta 2}$ C-K factors*

Elemennt	**E (keV)**	**$K_{\beta 1}$**	**E (keV)**	**$K_{\beta 2}$**
Sm	7.649	1.020	11.372	1.155
Eu	7.649	1.016	11.372	1.131
Bi	15.859	1.019	16.896	1.108

Theoretical calculations reveal that when the direct ionizations of individual *L* subshells are considered separately, C-K transitions lead to a substantial enhancement in X-ray production. According to the

theoretical results presented in Tables 5 and 6, C-K (The theoretical $K_{\alpha 1}$ and K_{l1}) factors result in an approximately 8.8% increase in *L*-shell X-ray intensities, while other related factors ($K_{\alpha 2}$and K_{l2})contribute an additional 30% increase.

The results given in Table 7 indicate that the CosterKronig factors have relatively smaller values. C-K (The $K_{\beta 1}$) factors result in an approximately 1.6-2% increase in *L*-shell X-ray intensities, while other related factors ($K_{\beta 2}$) contribute an additional 10.8-15% increase.

The obtained results further demonstrate that the influence of CK transitions strongly depends on both the atomic number and the excitation energy. At appropriate excitation energies, the efficient transfer of vacancies formed in the L_1 and L_2 subshells to the L_3 subshell leads to a pronounced enhancement of Lα X-ray intensities. In contrast, the more limited increase observed in L_β lines can be explained by the weaker influence of CK transitions on these lines.

In conclusion, it is evident that Coster–Kronig transitions enhance L-shell X-ray intensities, and neglecting this effect in quantitative XRF analyses may lead to systematic errors. Therefore, CK transitions must be explicitly taken into account in high-precision XRF measurements, particularly for elements with medium and high atomic numbers.

CONCLUSION

The obtained results demonstrate that the photoionization probability of *L*-subshell characteristic X-rays increases with increasing atomic number. This increase in atomic number reduces the

energy separations between the L subshells, thereby enhancing the probability of Coster–Kronig transitions and consequently increasing the number of vacancies created in the L_3 subshell. This mechanism constitutes the fundamental physical reason for the observed enhancement, particularly in the intensities of the Lα lines. According to the present findings, the presence of non-radiative (radiationless) transitions leads to significant variations in the measured X-ray intensities, and neglecting this effect in quantitative XRF analyzes may result in systematic errors. Therefore, in L-shell X-ray analyzes of elements, the influence of Coster–Kronig transitions must be taken into account together with the photoionization processes.

REFERENCES

Barrea, R. A., Pérez, C. A., & Sánchez, H. J. (2004). Barium L subshells Coster–Kronig and fluorescence yields by the subshell selective photoionization method. *Nuclear Instruments and Methods in Physics Research Section B: Beam Interactions with Materials and Atoms*, *215*(3-4), 308-316.

Bonzi, E. V., & Badiger, N. M. (2006). Measurement of L subshell fluorescence yields of elements in the range $45 \leqslant Z \leqslant 50$ using synchrotron radiation. *Nuclear Instruments and Methods in Physics Research Section B: Beam Interactions with Materials and Atoms*, *248*(2), 242-246.

Chauhan, Y., Tiwari, M. K., & Puri, S. (2008). Li (i= 1–3) subshell X-ray production cross sections and fluorescence yields for some elements with $56 \leqslant Z \leqslant 68$ at 22.6 keV. *Nuclear Instruments and*

Methods in Physics Research Section B: Beam Interactions with Materials and Atoms, *266*(1), 30-36.

Coster, D., & Kronig, R. D. L. (1935). New type of auger effect and its influence on the x-ray spectrum. *Physica*, *2*(1-12), 13-24.

Ertugrul, M. (2001). Measurements of L_{3l}, $L_{3\alpha}$, $L_{3\beta}$, $L_{2\beta}$, $L_{2\gamma}$, $L_{1\beta}$ and $L_{1\gamma}$ X-ray production cross-sections for Tl, Pb and Bi elements at 59.5 keV. *Nuclear Instruments and Methods in Physics Research Section B: Beam Interactions with Materials and Atoms*, *179*(4), 459-464.

Ertugrul, M. (2002). Measurement of L subshell production cross-section and Coster–Kronig transition probability (f_{12}) for Hg and Au elements at the 59.5 keV. *Journal of Quantitative Spectroscopy and Radiative Transfer*, *72*(5), 567-574.

Elam, W. T., Ravel, B. D., & Sieber, J. R. (2002). *X-ray absorption and emission energies of the elements*. *Radiation Physics and Chemistry,* 63(2), 121–128

Hubbell, J. H., Trehan, P. N., Singh, N., Chand, B., Mehta, D., Garg, M. L., ... & Puri, S. (1994). A review, bibliography, and tabulation of K, L, and higher atomic shell x-ray fluorescence yields. *Journal of Physical and Chemical Reference Data*, *23*(2), 339-364.

Jenkins, R. (1974). An introduction to X-ray spectrometry

Kaya, A., & Ertugrul, M. (2003). Measurement of L X-ray production cross sections and Li subshell fluorescence yields. *Journal of electron spectroscopy and related phenomena*, *130*(1-3), 111-118.

Krause, M. O., Nestor Jr, C. W., Sparks Jr, C. J., & Ricci, E. (1978). *X-ray fluorescence cross sections for K and L x rays of the elements* (No. ORNL-5399). Oak Ridge National Lab.(ORNL), Oak Ridge, TN (United States).

Krause, M. O. (1979). Atomic radiative and radiationless yields for K and L shells. *Journal of physical and chemical reference data*, *8*(2), 307-327.

Mann, K. S., Singh, N., Mittal, R., Sood, B. S., & Allawadhi, K. L. (1994). Ll, Lα, Lβ and Lγ X-Ray Production Cross-Sections in Elements 57≤ Z≤ 92 by 8–50 ke V Photons. *X-Ray Spectrometry*, *23*(5), 208-217.

Manoj, S. P., & Sripathi Punchithaya, K. (2025). K shell fluorescence parameters of low atomic numbered transition elements using Au-L α X-rays. *Radiation Physics and Chemistry*, *235*, 112859.

Meddouh, K., Daoudi, S., Kahoul, A., Sampaio, J. M., Marques, J. P., Parente, F., ... & Hamidani, A. (2023). Average K-, L-, and M-shell fluorescence yields: A new semi-empirical formulae. *Radiation Physics and Chemistry*, *202*, 110481.

Ménesguen, Y., & Lépy, M. C. (2020). Experimental determination of L fluorescence yields of gadolinium. *X-Ray Spectrometry*, *49*(5), 596-602.

Miranda, J., de Lucio, O. G., Téllez, E. B., & Martınez, J. N. (2004). Multiple ionization effects on total L-shell X-ray production cross sections by proton impact. *Radiation Physics and Chemistry*, *69*(4), 257-263.

Nica, N., Hardy, J. C., Iacob, V. E., Montague, J. R., & Trzhaskovskaya, M. B. (2005). Precise measurement of K-shell fluorescence yield in iridium: An improved test of internal-conversion theory. *Physical Review C—Nuclear Physics*, *71*(5), 054320.

Ohno, M. (2004). The effect of Coster–Kronig transition on the Auger-photoelectron coincidence spectroscopy spectra of early 3d-transition metals. *Journal of electron spectroscopy and related phenomena*, *136*(3), 221-228

Öz, E., Ekinci, N., Özdemir, Y., Ertugrul, M., Sahin, Y., & Erdogan, H. (2001). Measurement of atomic L shellCoster-Kronig yields (f_{12}, f_{23} and f_{13}) for someelements in the atomic number range

59⩽ Z⩽ 90. *Journal of Physics B: Atomic, Molecular and Optical Physics*, *34*(4), 631.

Öz, E., Şahın, Y., & Ertuğrul, M. (2004). Measurements of Coster–Kronig enhancement factors of some elements in the atomic number range 74⩽ Z⩽ 90. *Radiation Physics and Chemistry*, *69*(1), 17-21.

Raulo, A., Grassi, D., & Perillo, E. (2007). L3-subshell x-ray emission rates for Dy and Ho. *Journal of Physics B: Atomic, Molecular and Optical Physics*, *40*(13), 2739.

Scofield, J. H. (1972). *Theoretical photoionization cross sections from 1 to 1500 keV* (No. UCRL--51326). California Univ., Livermore. Lawrence Livermore Lab..

Scofield, J. H. (1969). Radiative decay rates of vacancies in the K and L shells. *Physical Review*, *179*(1), 9.

Scofield, J. H. (1976). Hartree-Slater subshell photoionization cross-sections at 1254 and 1487 eV. *Journal of electron spectroscopy and related phenomena*, *8*(2), 129-137.

Sahnoune, Y., Kahoul, A., Daoudi, S., Sampaio, J. M., Aylikci, N. K., Aylikci, V., ... & Medjadi, D. E. (2020). Updated database, new empirical and theoretical values of average L shell fluorescence yields of elements with 23≤ Z≤ 96. *Radiation Physics and Chemistry*, *166*, 108495.

Söğüt, Ö., Büyükkasap, E., Küçükönder, A., Ertuğrul, M., & Erdoğan, H. (2002). Determination of Coster–Kronig transition probabilities (L1→ L2, L1→ L3 and L2→ L3) for Hg and Bi in molecules. *X-Ray Spectrometry: An International Journal*, *31*(1), 71-74.

Şimşek, Ö. (2001). L_2 sub-shell Coster–Kronig yield at Z= 76 and 81. *Nuclear Instruments and Methods in Physics Research Section B: Beam Interactions with Materials and Atoms*, *173*(3), 269-274.

Turhan, M. F., Akman, F., Kaçal, M. R., & Durak, R. (2017). Measurements of K X-ray fluorescence cross-sections, fluorescence yields, level widths and radiative vacancy transition probabilities for the elements Zr, Mo, Cd, Er at 59.54 keV. In *IOP Conference Series: Materials Science and Engineering* (Vol. 282, No. 1, p. 012015). IOP Publishing.

Unterumsberger, R., Hönicke, P., Colaux, J. L., Jeynes, C., Wansleben, M., Müller, M., & Beckhoff, B. (2018). Accurate experimental determination of Gallium K-and L3-shell XRF fundamental parameters. *Journal of Analytical Atomic Spectrometry*, *33*(6), 1003-1013.

CHAPTER 2

EVALUATION OF EXCHANGE BIAS STUDIES: CURRENT SITUATION ANALYSIS AND FUTURE TRENDS

1. Taner KALAYCI [1]
2. Muhammet ARUCU [2]

1-Introduction

In the context of spintronics, exchange bias—a phenomenon of basic and technological relevance in magnetic materials—plays a significant role. A method to ascertain and control a material's magnetism is by exchange bias, an effect that arises at the contact between two distinct magnetic materials. This phenomenon is used in many technological applications, such as magnetic random-access memory (MRAM), hard drives, and sensors.

[1] Assoc. Prof. Dr., Department of Medical Services and Techniques, Bandırma Onyedi Eylül University, Bandırma, 10200, Balıkesir, Türkiye Unvan, Kurum,Bölüm, Orcid: 0000-0002-6374-2373

[2]Assist. Prof. Dr., Department of Computer Technologies, Bandırma Onyedi Eylül University, Gönen, 10900, Balıkesir, Türkiye, Orcid: 0000-0001-7620-9044

When a cooling process is applied above the Neel temperature (T_N) of the AFM material in hybrid systems with ferromagnetic (FM) and antiferromagnetic (AFM) layers, the FM layer experiences directional magnetic anisotropy [1-3]. The exchange bias interaction at the FM/AFM interface is the cause of this anisotropy. Meiklejohn and Bean first noticed exchange bias in 1956 while studying Co particles coated with natural CoO [4]. This effect is also present in thin films [6], AFM single crystals [5], and other heterogeneous magnetic systems, according to later research. Additionally, the exchange bias effect is significant in applications like magnetic recording media [8], permanent magnets [7], and anisotropic magnetoresistance-based recording heads [9]. The exchange bias energy at the interface in the Meiklejohn and Bean model allows the AFM layer to stabilize the ferromagnetic layer's magnetic orientation [10]. However, this classical model has proven to be inadequate due to spin irregularities, grain boundaries, and roughness present in real systems. As a result, more sophisticated models also take into account ideas like spin glass-like structures, frozen spins, and field-cooled states [3].

Exchange bias is employed to maintain the magnetic orientation of the reference layer in devices such as magnetic tunnel junctions, spin valve topologies, and MRAMs [11]. This feature improves data dependability and ensures steady device operation. Furthermore, exchange bias has been seen not only in typical FM/AFM interfaces but also in ferrimagnetic, multilayer, and even single-phase nanostructures [6]. This suggests that the exchange bias phenomena may be related to more complex and general spin configurations.

This study uses bibliometric analysis techniques to look at exchange bias research that has been published in the Web of Science (WoS) database. Prominent publications, authors, institutions,

nations, and co-authorship are assessed, along with the field's historical evolution and status. The basic issues and difficulties that arise in exchange bias research in magnetic applications are also discussed. The results contribute to the future of spintronic devices and show current trends in the field of exchange bias.

2. Methods

Using the search term "exchange bias," 6835 scholarly works were found in the WoS database. By examining each publication in this database, an attempt was made to shed light on the history, current state, and whether " exchange bias " has been extensively researched in the literature. This section addresses all research on " exchange bias" and offers a fresh perspective.

3. Data Analysis, Document Collecting

The main topic of this section is the examination of articles related to "exchange bias" in the WoS database. As of December 4, 2025, a WoS database search using the terms "exchange bias" or "exchange-bias" yielded a total of 6835 results. The search was filtered by document type to include only english-language and only research articles. For bibliometric analysis, these articles were downloaded as tab-delimited files (Win format) containing full records. Subsequently, the VOSviewer program was used to perform analyses such as most frequently used keywords, abstracts, citation patterns, and co-authorship.

4. Results and Discussion

Figure 1 shows that research articles on "exchange bias" are mostly found in fields such as Physics, Materials Science, Engineering, and Chemistry, while Figure 2 shows an increasing trend over the years.

Figure 1. Number of "exchange bias" by research areas

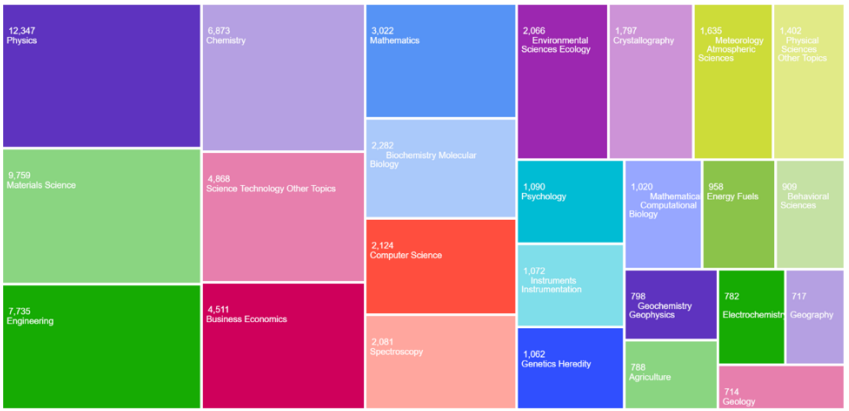

Figure 2. Number of "exchange bias" articles by year

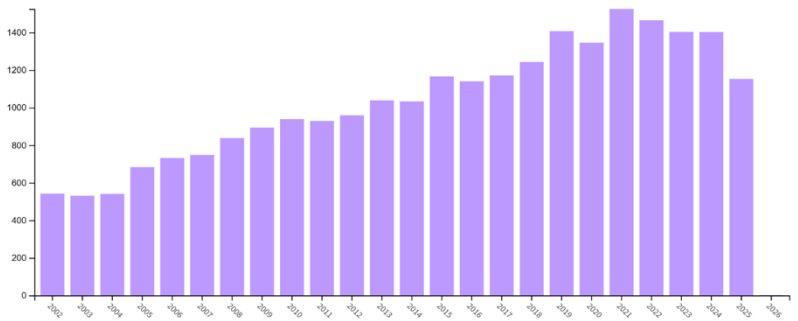

4.1. Co-authorship - Authors Analysis

Figure 3. The graph of "co-authorship - Author" analysis

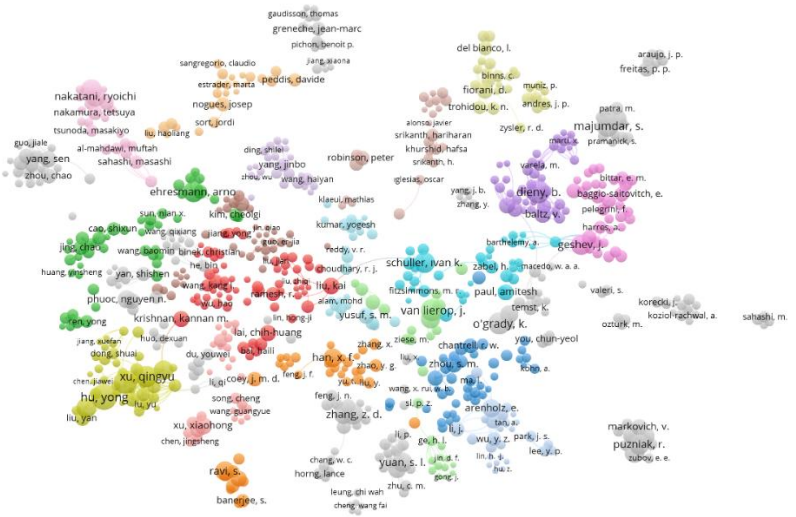

The co-authorship analysis reveals collaborations in "exchange bias" research, researcher profiles, and co-publication trends. This analysis shows that 18,881 authors have contributed to the field through journal publications. In the bibliometric analysis, when the threshold of at least 3 publications and at least 10 citations is applied, 3,212 authors meet these criteria. Table 1 lists the authors with the most publications in order. The top three are: Hu, Yong (52 publications), Dieny, B. (44 publications), and Du Jun (42 publications). Based on this data, the most prolific authors have been identified. Figure 3 shows the distribution of authors. In the figures, the bubble and font sizes represent the number of publications by the authors, and the bubble colors represent clusters formed by co-authorship relationships.

Table 1. Top ten authors with the greatest documents

Author	Documents
Hu, Yong	52

Dieny, B.	44
Du Jun	42
Van Lierop, J	39
Majumbar S.	39
O'grady, K.	38
Giri S.	37
Xu Qingyu	35
Zhang Z.D.	33
Nakatani Ryoichi	33

4.2. Co-authorship - Affiliations Analysis

Looking at the results of the co-authorship analysis at the institution level, it has been revealed that many institutions contribute to this field through journal publications. In this part of the study, when a threshold of at least 5 publications and at least 5 citations was set, it was seen that 643 out of 3003 authors met this condition. According to the information presented in detail in Table 2, Chinese Acad Sci stands out as the institution with the highest productivity with 337 publications. Chinese Acad Sci is followed by Nanjing University (177), Tohoku University (120), Indian Institute of Technology (115), National University of Singapore (110), and University of California Berkeley (106). These institutions are among the leading contributors to research on exchange bias. Figure 4 illustrates the distribution among these institutions. The connecting lines between the institutions show the intensity of the collaboration and visually represent global research partnerships in the field of exchange bias.

Figure 4. The graph of "co-authorship - Affiliations" analysis

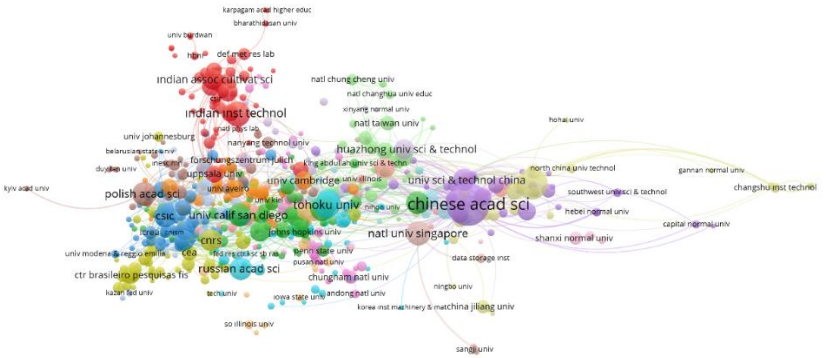

Table 2. Top ten institutions with the highest documents, citations and total link strength

Institutions	Documents	Citations	Total Link Strength
chinese acad sci	337	16	38
cnrs	90	452	16
csıc	96	136	13
nanjing univ	177	76	36
natl univ singapore	110	971	10
northeastern univ	93	864	15
polish acad sci	102	127	5
russian acad sci	94	649	5
tohoku univ	120	49	10
univ calif berkeley	106	335	19
univ calif san diego	100	52	11

univ york	102	79	14
ındian ınst technol	115	53	6

4.3. Co-authorship - Countries Analysis

Looking at the results of the co-authorship analysis at the country level, it has been revealed that many countries contribute to this field through journal publications. In this part of the study, when a threshold of at least 3 publications and at least 10 citations was set, it was seen that 71 out of 91 authors met this condition. According to the information presented in detail in Table 3, China stands out as the institution with the highest productivity with 1542 publications. China is followed by USA (1267), India (826), Germany (741), France (493), and Japan (404). These countries are among the leading contributors to research on exchange bias. Figure 5 illustrates the distribution among these countries. The connecting lines between the countries show the intensity of the collaboration and visually represent global research partnerships in the field of exchange bias.

Figure 5. The graph of "co-authorship - Countries" analysis

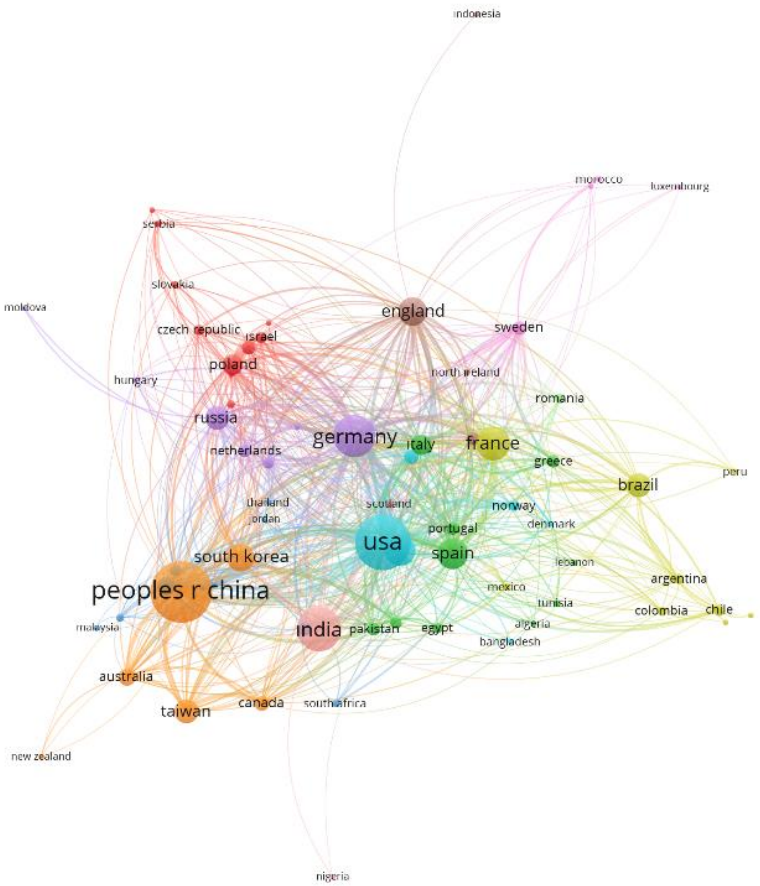

Table 3. Top twenty countries with the highest documents, citations and total link strength

Countries	Documents	Citations	Total Link Strength
Australia	124	50	152
Brazil	233	1338	118

Canada	101	3324	138
England	331	1120	310
France	493	245	450
Germany	741	123	590
Japan	404	1394	222
peoples r china	1542	4208	526
Poland	176	1532	130
Russia	247	1083	178
Singapore	146	199	94
South Korea	311	111	198
Spain	386	2456	411
Sweden	87	416	131
Switzerland	92	265	137
Taiwan	242	769	217
Türkiye	80	9550	32
USA	1267	504	859
India	826	16162	267
Italy	168	21963	172

4.4. Co-occurences – Author Keywords

The keyword co-occurrence map in VOSviewer examines the relationships between keywords, offering a valuable tool for researchers to identify key concepts and how these concepts interconnect to form sub-domains, which may represent emerging

research hotspots. The keyword "exchange bias," with 783 total occurrences, has the highest total link strength of 5321, indicating that it frequently co-occurs with other keywords. Figure 6 shows the keyword co-occurrence map for exchange bias publications, where "exchange bias" most often co-occurs with "exchange-bias" as evidenced by the widest bubble and the highest link strength of 3343.

Figure 6. The Graph of "Co-occurences – Author Keywords" analysis

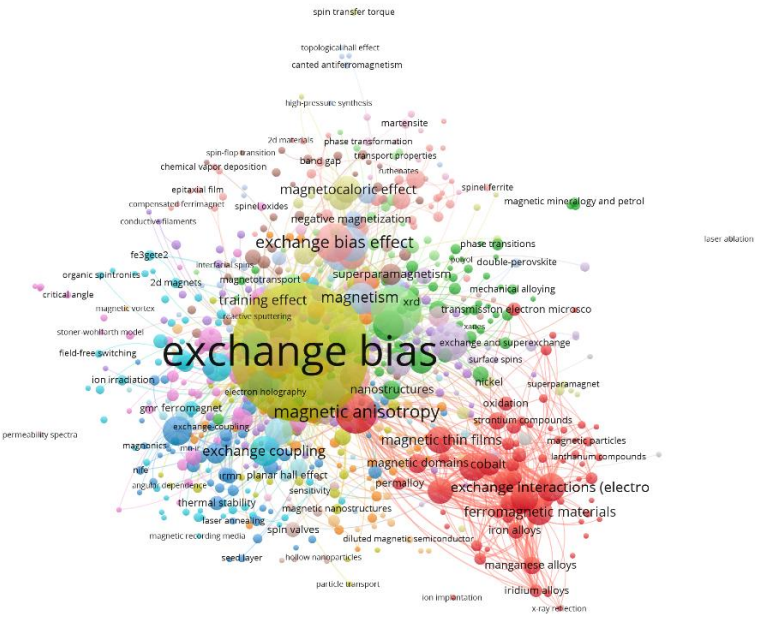

4.5. Citation – Documents Analysis

According to the citation analysis, 6335 sources contributed to the field of exchange bias; 1473 of these sources received at least 25 citations. Berkowitz (1999) is the most cited document, as shown in the largest pistachio green in the document network map in Figure 7. Furthermore, Berkowitz (1999) has the strongest linkage with other articles, as seen with the highest total linkage strength (254).

The top three documents in terms of total linkage strength, number of citations, and document number are:

Berkowitz (1999) – Total linkage strength: 254; Citations: 1532, Koon (1997) – Total linkage strength: 152; Citations: 745, Nogues (1996b) - Total linkage: 126; Citations: 524

Figure 7. The Graph of "Citation – Documents" Analysis

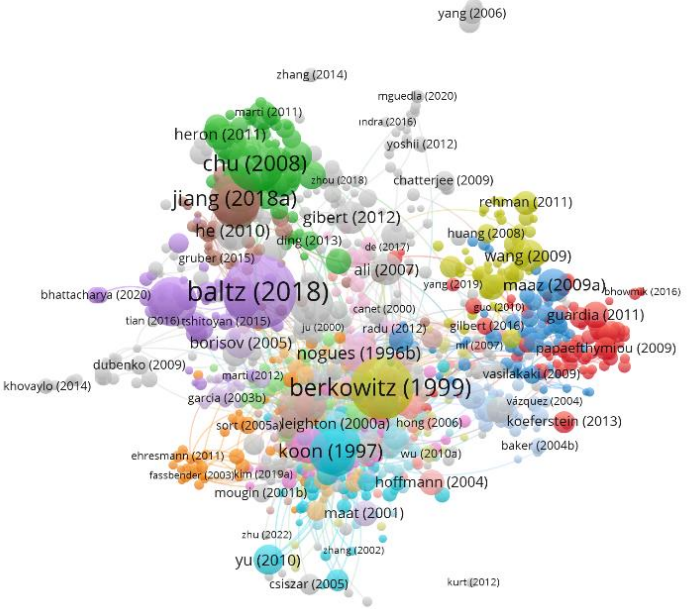

4.6. Citation – Source Analysis

According to the citation analysis of publication sources, 468 sources contributed to the field of exchange bias; 174 of these sources published three articles with at least ten citations. As can be seen from the largest light blue bubble in the network map of source citations in Figure 8, the most cited journal is Physical Review B. In

addition, the Journal of Magnetism and Magnetic Materials has the highest overall linkage strength (5006), indicating its central role in the citation network and its significant connection with other publications. This strong linkage strength reflects how frequently exchange bias is mentioned in various journals, demonstrating its widespread impact within the scientific community. The top three sources by total linkage strength, number of citations, and number of documents are as follows:

Journal of Applied Physics – Total linkage strength: 3750; Citations: 12828; Papers: 768, Journal of Magnetism and Magnetic Materials – Total linkage strength: 5006; Citations: 10770; Documents: 689, Physical Review B - Total linkage: 3576; Citations: 22959; Documents: 617

Figure 8. The Graph of "Citation – Source" Analysis

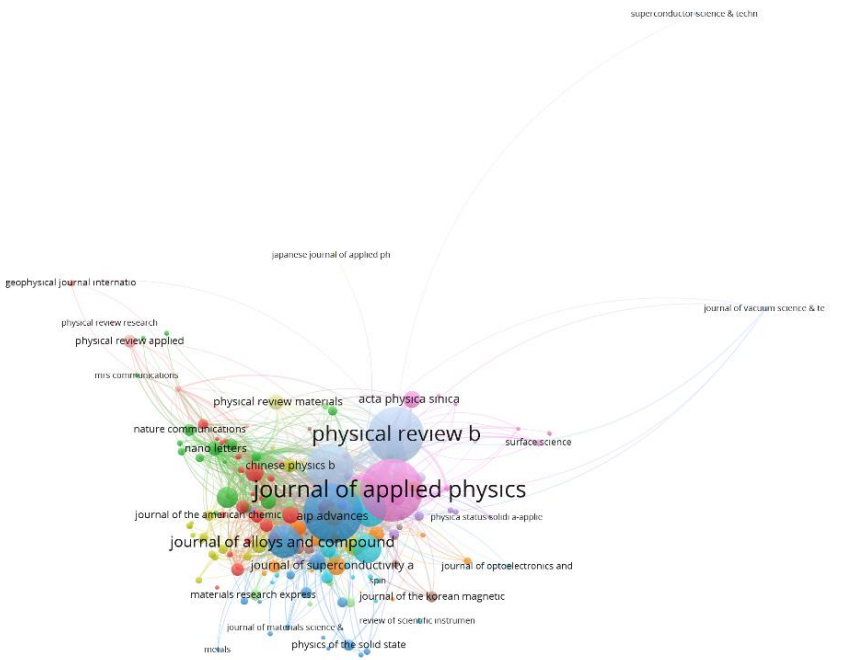

4.7. Citation – Affiliations Analysis

Looking at the citation analysis of links on exchange bias results; 3003 institutions have contributed to the field of Exchange Bias; 362 of these have published at least 10 articles with at least 10 citations. As shown in one of the blue bubbles in the link citation network map of cross-country citations in Figure 9, the most cited institution is the University of California, Berkeley. In addition, the University of California, San Diego has the highest total link strength (4523), demonstrating both its significant role in the citation network and its substantial linkage to other publications. This strong link strength reflects how frequently exchange bias is mentioned across various journals, showing its widespread impact within the scientific community. The top 3 institutions in terms of article count, citation count, and total link strength are as follows:

Univ Calif San Diego – Total linkage strength: 4523; Citations: 7766; Documents: 100, Univ Calif Berkeley – Total linkage strength: 2426; Citations: 10046; Documents: 106, Chinese Acad Sci - Total linkage: 2756; Citations: 7022; Documents: 337

Figure 9. The Graph of "Citation – Affiliations" Analysis

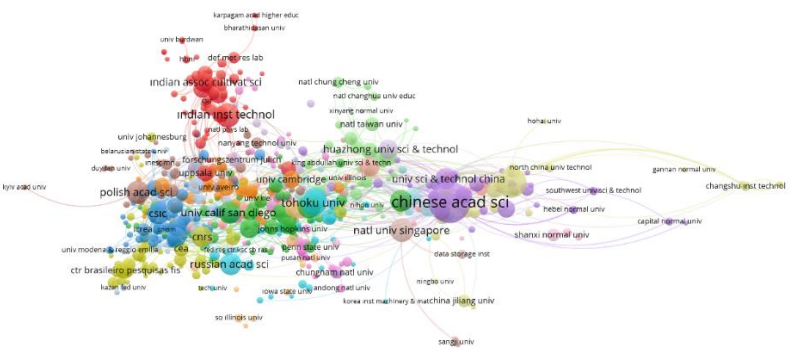

4.8. Citation – Countries Analysis

Looking at the citation analysis results; 94 countries have contributed to the field of Exchange Bias; 71 of these have published at least 3 articles with at least 10 citations. As shown in the orange bubble on the network map of cross-country citations in Figure 10, the most cited country is the USA. China has the most articles (1542), demonstrating its close ties with other journals and its key position in the citation network. The top 3 countries in terms of article count, citation count, and total link strength are as follows:

USA – Total linkage strength: 14323; Citations: 53845; Documents: 1267, China – Total linkage strength: 9293; Citations: 25710; Documents: 1542, Germany - Total linkage: 6755; Citations: 21963; Documents: 741

Figure 10. The Graph of "Citation – Countries" Analysis

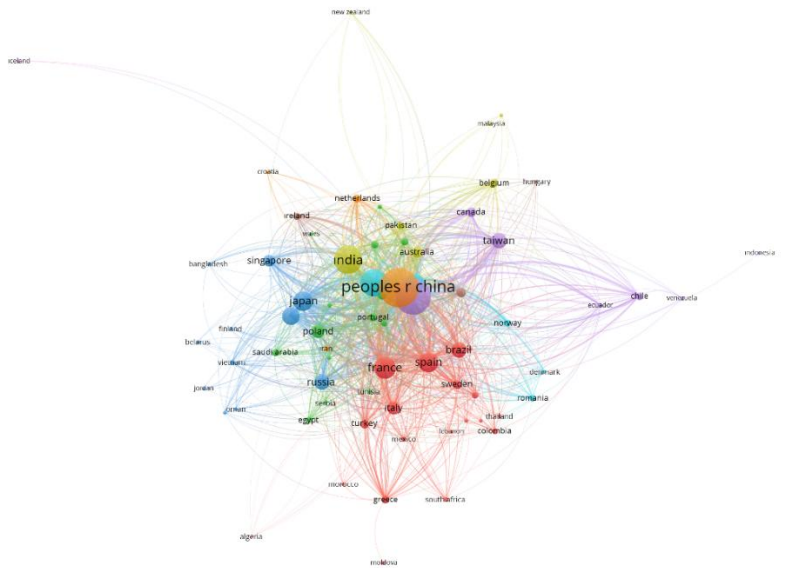

4.9. Co-citation analysis of cited references

In the co-citation analysis of cited references, the minimum number of citations for a cited reference was entered as 20. Of the total 80780 cited references, 1224 meet this condition. As shown in Figure 11, it consists of a total of 5 clusters. Cluster 1 consists of 355, cluster 2 of 278, cluster 3 of 210, cluster 4 of 131, and cluster 5 of 26 cited reference, and these clusters are colored red, green, blue, yellow, and purple, respectively.

Figure 11.The Graph of " Co-citation - cited references" analysis

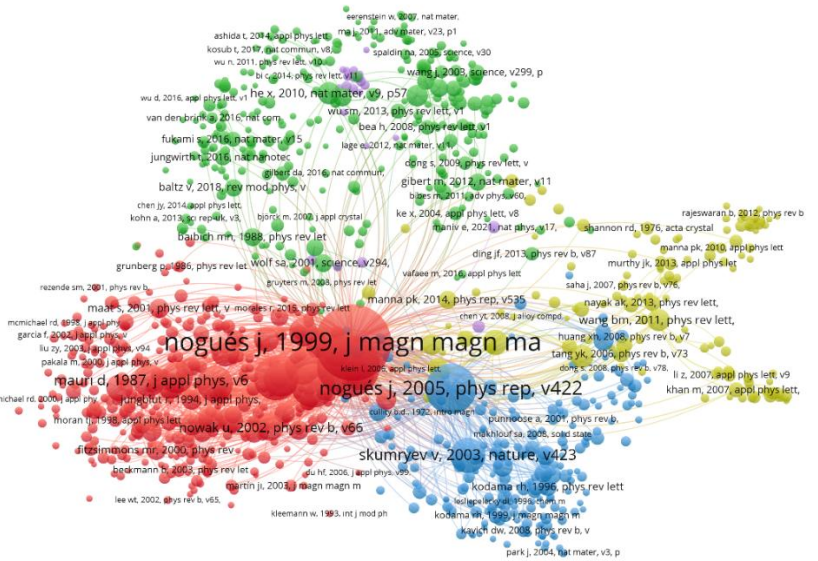

4. Conclusion

The results of the bibliometric analysis reveal that some researchers are leading the way in this field. Citation numbers and co-authorship networks show that researchers like Hu Yong have made significant contributions to the Exchange Bias literature, contributing to both the development of theoretical models and the advancement of empirical validations.

Institutional analyses show that exchange bias studies are conducted at universities and research centers. Organizations such as the Chinese Academy of Sciences and CNRS are considered pioneers in this field due to their high number of publications and citations. When viewed on a country basis, exchange bias research has become widespread worldwide. While India, China, and the US stand out in terms of publication numbers and international collaborations, developing countries have shown progress toward a more balanced and multifaceted structure in recent years.

Bibliometric analysis results show that, despite the exchange bias field not being very old, it is a well-established and dynamic area of research. The increase in the number of publications, the diversity of topics, and the rise in international collaborations indicate that scientific output will continue to grow in the coming years. It is predicted that the exchange bias phenomenon will maintain its importance in both fundamental science and advanced technological applications, particularly in conjunction with developments in spintronics, magnetic data storage, and quantum technologies.

References

J. Nogués and I. K. Schuller, "Exchange bias," *Journal of Magnetism and Magnetic Materials*, vol. 192, pp. 203–232, 1999.

[2] A. E. Berkowitz and K. Takano, "Exchange anisotropy — a review," *Journal of Magnetism and Magnetic Materials*, vol. 200, pp. 552–570, 1999.

[3] M. Kiwi, "Exchange bias theory," *Journal of Magnetism and Magnetic Materials*, vol. 234, pp. 584–595, 2001.

[4] W. H. Meiklejohn and C. P. Bean, “New magnetic anisotropy,” *Physical Review*, vol. 102, no. 5, p. 1413, 1956.

[5] R. L. Stamps, “Mechanisms for exchange bias,” *Journal of Physics D: Applied Physics*, vol. 33, no. 23, pp. R247–R268, 2000.

[6] J. Nogués et al., “Exchange bias in nanostructures,” *Physics Reports*, vol. 422, pp. 65–117, 2005.

[7] E. Kneller and R. Hawig, “The exchange-spring magnet: A new material principle for permanent magnets,” *IEEE Transactions on Magnetics*, vol. 27, pp. 3588–3560, 1991.

[8] S. Chikazumi, *Physics of Ferromagnetism*, 2nd ed., Oxford University Press, 1997.

[9] R. C. O’Handley, *Modern Magnetic Materials: Principles and Applications*, Wiley, 2000.

[10] W. H. Meiklejohn and C. P. Bean, “Anisotropy effects associated with magnetic ordering in antiferromagnetic-ferromagnetic systems,” *Physical Review*, vol. 105, p. 904, 1957.

[11] S. S. P. Parkin, K. P. Roche, M. G. Samant et al., “Exchange-biased magnetic tunnel junctions and spin-valves,” *Journal of Applied Physics*, vol. 85, pp. 5828–5833, 1999.

CHAPTER 3

EFFECTS OF ARTIFICIAL INTELLIGENCE ON ANTENNA DESIGN, SIMULATION, AND MANUFACTURING PROCESSES

ERKAN TETİK[1]

Introduction

Antennas, as a cornerstone of wireless communication, play a pivotal role in our modern world. Their remarkable ability to convert radio waves into electrical signals and vice versa has rendered them indispensable components across a vast spectrum of applications, ranging from mobile telephony and satellite communication to radar systems and the Internet of Things (IoT) [1–7]. The history of antenna technology commenced with Guglielmo Marconi's invention of wireless telegraphy in the late 19th century and has since undergone continuous evolution. This developmental trajectory, spanning from rudimentary dipole antennas to advanced microstrip, patch, array, and smart antennas, has been shaped by persistent demands for increased bandwidth, higher efficiency, reduced form factors, and enhanced functionality [8–13]. Presently, emerging domains such as 5G and beyond communication systems,

[1] Assoc. Prof. Dr., Usak University, Department of Instructional Technologies, Orcid: 0000-0002-8183-8141

autonomous vehicles, sophisticated healthcare technologies, and space exploration necessitate further advancements in antenna performance and adaptability [14–17]. While traditional antenna design, simulation, and manufacturing processes have witnessed significant progress over the years, they inherently remain time-consuming, iterative, and computationally intensive. During the design phase, engineers typically leverage analytical equations and numerical optimization techniques. The simulation process aims to predict antenna performance through powerful electromagnetic (EM) solvers, including the finite element method (FEM), finite-difference time-domain (FDTD), and method of moments (MoM). These simulations are critically important for design verification prior to physical prototyping. However, modern requirements such as complex antenna structures, multiple frequency bands, and stringent spatial constraints increasingly challenge the limits of conventional methodologies. Furthermore, manufacturing processes often entail engineering complexities related to precise material selection, production tolerances, and assembly stages, which can incur substantial costs and lead times [18–22].

The rapid proliferation of artificial intelligence (AI) and machine learning (ML) has triggered a paradigm shift, fundamentally transforming engineering and telecommunications landscapes. In contrast to traditional physics-based or empirical models reliant on closed-form equations, ML algorithms distinguish themselves by their ability to autonomously extract patterns and statistical correlations from large datasets. This data-driven capability enables the resolution of high-dimensional problems that are often computationally intractable for conventional methods [23]. Consequently, these techniques are redefining the lifecycle of complex systems through robust prediction, automated decision-making, and sophisticated optimization. Within the telecommunications sector, this impact is evident in the deployment

of self-organizing networks (SONs), predictive channel estimation, and intelligent signal classification [24,25]. Broader engineering disciplines are similarly leveraging AI to accelerate innovation, ranging from generative design in mechanical engineering to predictive maintenance and process control in smart manufacturing [26,27]. Collectively, these capabilities have paved the way for AI's integration into antenna engineering, offering novel solutions to the limitations of traditional design, simulation, and manufacturing paradigms [28,29].

The primary objective of this chapter is to investigate the paradigm shift brought by artificial intelligence in antenna design, simulation, and manufacturing. Specifically, it addresses AI's capability to optimize antenna performance, solve high-complexity EM problems, and enhance efficiency within manufacturing workflows. The text thoroughly discusses both the promising opportunities and the significant challenges associated with this technological integration. In terms of scope, the chapter bridges the gap between machine learning theories (supervised, unsupervised, RL, and DL) and their practical applications, such as parametric optimization, surrogate modeling, and fault diagnosis. Concluding with a visionary outlook, the chapter underscores the central role AI is poised to play in the next generation of antenna technologies.

2. The Role of Artificial Intelligence in Antenna Design

Although firmly rooted in established EM theory, the traditional antenna design workflow remains a fundamentally iterative and heuristic process. Typically, the design phase initiates with an analytical model or a canonical topology, followed by a rigorous cycle of parametric tuning, high-fidelity full-wave simulation, and performance assessment. However, this methodology encounters severe scalability and efficiency bottlenecks when addressing the stringent requirements of modern

wireless ecosystems. Demands for multi-band operation, wide bandwidth, miniaturization, and reconfigurability have expanded the design space into high-dimensional, complex territories [30]. Navigating this complexity via conventional trial-and-error approaches is not only computationally prohibitive but also restricts the discovery of non-intuitive, unconventional geometries [31]. The advent of AI, and specifically Machine Learning (ML), heralds a paradigm shift, transitioning the field from laborious iteration to data-driven automation. By exploiting statistical patterns, AI facilitates rapid surrogate modeling and inverse design capabilities [32]. Consequently, rather than relying on exhaustive brute-force simulations, AI-driven frameworks enhance design efficiency, offering real-time performance prediction and the generative creation of novel antenna structures based on specific performance criteria [33].

Figure 1 AI-Driven Antenna Design Workflow

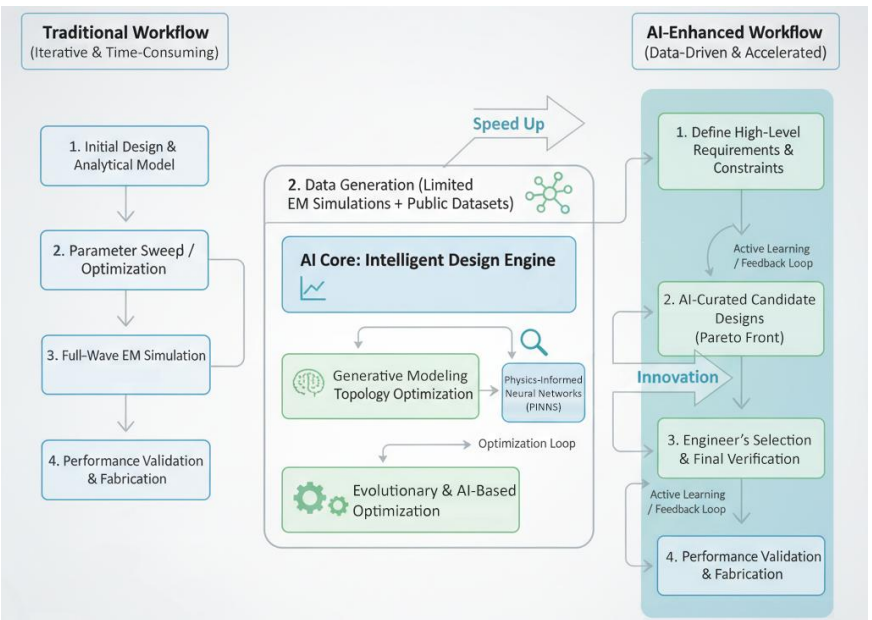

Fig. 1 illustrates the transformative impact of AI on the antenna design process, contrasting the conventional, iterative workflow with an AI-enhanced, data-driven approach. The Traditional Workflow (left panel) depicts a linear and often time-consuming sequence involving initial design, parameter scans, and extensive, high-fidelity EM simulations. The AI-enhanced workflow (right panel) begins with defining requirements. This is followed by an automated design and optimization phase driven by an AI core, the Intelligent Design Engine. This core uses various AI techniques, such as generative modeling and topology optimization, to create novel structures. It also uses physics-informed neural networks (PINNs) to rapidly and accurately model. The evolutionary and AI-based optimization module, often assisted by surrogate models, significantly speeds up the exploration of design parameters. The AI system provides a set of candidate designs that facilitate informed decision making. Ultimately, this process shift enables rapid optimization, accelerated simulation, high-accuracy modeling of complex structures, and a largely automated design exploration, thereby significantly reducing design cycles and fostering the discovery of advanced antenna solutions.

2.1. Rapid Optimization of Antenna Parameters

One of the most laborious phases in antenna engineering is the optimization of geometric and material parameters to satisfy stringent performance targets, such as resonant frequency, impedance matching (S_{11} < -10 dB), gain, bandwidth, and radiation pattern characteristics. Traditional, gradient-based methods are at risk of becoming trapped in local minima within the complex, multimodal landscapes of antenna performance metrics. Conversely, simple parameter sweeps suffer from the "curse of dimensionality," rendering them computationally prohibitive as the number of design variables increases. Artificial Intelligence offers a robust suite of

alternatives to these limitations, primarily through Evolutionary Algorithms (EAs) and Surrogate-Model-Assisted Optimization [34].

EAs, techniques like Genetic Algorithms (GAs) and Particle Swarm Optimization (PSO) are inspired by natural processes. A GA, for instance, maintains a "population" of potential antenna designs (individuals), each defined by a set of parameters (genes). The performance of each design is evaluated using a "fitness function," which is typically derived from EM simulation results. Through processes mimicking natural selection, such as crossover (combining parameters from successful designs) and mutation (randomly altering parameters), the population evolves over generations toward optimal solutions [35,36].

While EAs are effective global optimizers, they inherently require a vast number of fitness evaluations, each potentially triggering a time-consuming EM simulation. To mitigate this computational burden, AI-driven surrogate modeling (also referred to as metamodeling) is employed. This approach involves training a Machine Learning model, such as a Deep Neural Network (DNN), Support Vector Machine (SVM), or Gaussian Process (Kriging), using a sparse dataset of antenna parameters and their corresponding EM responses. Once trained, the surrogate acts as a computationally efficient proxy for the full-wave solver. Optimization algorithms can then query this proxy thousands of times to rapidly explore the design space, drastically reducing the dependency on the physics-based simulator within the optimization loop [37,38].

2.2 Reduction of Simulation Times

High-fidelity full-wave EM simulation, utilizing numerical techniques such as FEM, Finite-Difference Time-Domain (FDTD), and Method of Moments (MoM), constitutes the standard verification protocol in modern antenna design [39]. However, this accuracy comes at a steep computational cost. A single simulation

for an electrically large or complex structure can necessitate hours—or even days—on high-performance computing clusters. This latency imposes severe constraints on the number of feasible design iterations, rendering large-scale global optimization practically unachievable. To circumvent this, AI-driven surrogate modeling has emerged as a primary solution. The fundamental strategy involves decoupling the expansive design exploration phase from the computationally intensive physics solver [40]. The process generally follows a three-stage workflow:

A Design of Experiments (DoE) methodology is employed to systematically sample the design space. A limited set of diverse antenna configurations (typically ranging from a few hundred to a few thousand) is simulated using the high-fidelity EM solver. This phase constructs a foundational dataset that maps specific design inputs (e.g., patch length, substrate height, feed coordinates) to their corresponding performance outputs. Subsequently, a Machine Learning model, most commonly a DNN, is trained on this generated dataset. The network learns to approximate the intricate, non-linear mapping functions between the antenna's physical geometry and its EM behavior. In cases involving image-like inputs, such as pixelated patch antenna layouts, Convolutional Neural Networks (CNNs) are particularly effective due to their ability to capture spatial feature dependencies. Once fully trained, the surrogate model functions as a real-time inference engine. It can predict the full performance spectrum, such as the complete curve across a frequency band or 3D radiation patterns, for any new set of design parameters within its training domain almost instantaneously. This approach effectively replaces the time-consuming physics simulation with a rapid prediction model, significantly accelerating the iterative design cycle.

2.3 High-Accuracy Modeling of Complex Antenna Structures

Contemporary antenna engineering deals with increasingly sophisticated structures that defy simple analytical characterization. These include metamaterial-inspired radiators, frequency-selective surfaces (FSS), densely packed phased arrays exhibiting significant mutual coupling, and reconfigurable antennas integrated with active components like PIN diodes or MEMS switches [41]. Modeling such architectures presents multifaceted challenges. In this context, AI provides robust tools that go beyond simple parameter estimation. These tools can solve complex physics problems and generate new topologies.

PINNs, a cutting-edge advancement involves embedding the governing physical laws directly into the machine learning architecture. PINNs are neural networks where the loss function incorporates not only the error between the model's prediction and the training data (data-driven loss) but also a residual term enforcing compliance with the underlying differential equations, such as Maxwell's equations. This "physics-informed" constraint ensures that the model's predictions remain physically consistent, even in regimes where training data is sparse or unavailable. For complex electromagnetic problems, PINNs can yield highly accurate surrogate models with significantly less training data compared to purely data-driven "black-box" approaches [42].

One revolutionary application of AI is inverse design. Rather than starting with geometry and working toward performance, inverse design begins with the desired performance (e.g., a specific radiation pattern or multiple frequency bands) and uses AI to generate a corresponding physical structure. Generative models like Generative Adversarial Networks (GANs) and Variational Autoencoders (VAEs) are exceptionally well-suited for this task. A GAN, for example, can be trained on a large dataset of antenna geometries and their performance characteristics. The "generator" network then learns to propose new, valid antenna layouts, while a

"discriminator" network assesses their quality. Through this adversarial process, the generator becomes adept at creating novel designs that meet specified high-level performance constraints [43].

3. AI Methodologies and Antenna Applications

While the preceding chapter established the transformative impact of AI on the antenna design paradigm, this chapter investigates the specific methodologies underpinning these advancements. It synthesizes ML, DL, and EAs under a unified computational framework. Although these categories possess distinct theoretical characteristics, their synergistic application has become increasingly prevalent in resolving complex engineering challenges. This section elucidates the fundamental mechanics of each technique and demonstrates their practical utility through relevant case studies. Special emphasis is placed on their capabilities in parameter estimation, performance prediction, global optimization, and generative design [44].

3.1. ML Based Methods

ML encompasses a diverse spectrum of algorithms capable of extracting patterns from data without explicit programming instructions. In the context of electromagnetics, these methods are particularly valuable for modeling the complex, non-linear mappings between antenna design parameters (geometry/materials) and their EM performance. They serve as robust engines for both parameter estimation and computationally efficient surrogate modeling.

Decision Trees (DTs) learn a sequence of simple decision rules inferred from the data features. While interpretable, individual DTs can be prone to overfitting. Support Vector Machines are powerful algorithms for classification and regression, particularly effective in high-dimensional spaces [45,46]. SVMs work by finding an optimal hyperplane that best separates different classes or fits data points with maximum margin. They are robust against overfitting

and can handle complex, non-linear relationships using kernel functions. RFs overcome the limitations of individual DTs by constructing an ensemble of many DTs during training. Each tree is trained on a random subset of the data and features, and the final prediction is an aggregation (e.g., majority vote for classification, average for regression) of individual tree predictions. This ensemble approach significantly improves accuracy, robustness, and reduces overfitting, making RFs highly effective for predicting antenna performance metrics.

Figure 2 Schematic representation of RF architecture. The model trains an ensemble of DTs on random subsets of data and aggregates their individual predictions (via majority voting for classification or averaging for regression) to produce a robust final output.

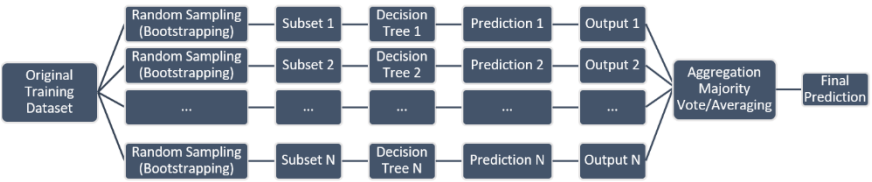

The architectural framework of RF algorithm is illustrated in Fig. 2. As depicted, the ensemble method aggregates the outputs of multiple independent DTs to derive a final prediction, thereby reducing the variance associated with individual estimators.

ML models excel in constructing high-speed surrogate models that map geometric parameters to performance characteristics (Forward Modeling) or, conversely, estimate required dimensions for a desired output (Inverse Modeling). For instance, algorithms can be trained to predict the resonant frequency of a microstrip patch given its substrate properties and dimensions with high fidelity. This predictive capability is critical for rapid design space exploration, enabling real-time feedback that traditional solvers cannot provide.

Consider the optimization of a patch antenna for maximum gain within specific form factor constraints. A dataset consisting of various patch dimensions (length, width, feed position, substrate height, dielectric constant) and their corresponding simulated gain values can be generated. An ML model, such as an RF Regressor, can then be trained on this dataset. Once the model learns the relationship, it can rapidly predict the gain for new, untested combinations of parameters. This surrogate model can be coupled with an external optimization algorithm, such as a simple gradient descent or an EA, to efficiently search the parameter space for configurations that yield the highest gain. This drastically reduces the number of computationally expensive full-wave EM simulations required [47].

3.2. DL for Antenna Design

DL, a specialized and sophisticated subset of ML, employs artificial neural networks with multiple processing layers (deep architectures) to learn hierarchical representations of data. Unlike traditional "shallow" learning methods that often require manual feature extraction, DL models are adept at processing high-dimensional raw data, such as antenna geometries represented as images or broadband frequency responses, and autonomously extracting salient features. This capability allows them to model complex electromagnetic phenomena with unprecedented accuracy [48].

CNNs are exceptionally powerful for processing grid-like data, making them ideal for analyzing antenna geometries represented as images or pixel maps. A CNN can be trained to directly predict the full 3D radiation pattern of an antenna simply by taking its 2D structural layout image as input. The convolutional layers automatically learn to detect relevant geometric features (e.g., slot shapes, trace widths, gaps) that influence the antenna's far-field

characteristics. This eliminates the need for explicit parameterization of the antenna and provides an ultra-fast alternative to full-wave simulations for pattern synthesis and analysis [49].

DNNs, with their multi-layered architecture, can capture highly complex, non-linear relationships between a multitude of antenna parameters and desired performance metrics. For bandwidth optimization, a DNN can be trained on a dataset comprising various antenna geometries (e.g., feed line width, ground plane dimensions, parasitic element placements) and their corresponding fractional bandwidths. The network learns how subtle changes in geometry impact the impedance matching over a frequency range. After training, the DNN can serve as a rapid predictor, allowing engineers to quickly iterate and identify configurations that yield wider bandwidths, a critical factor for modern wireless communication systems [50].

Transfer Learning is a powerful DL technique where a model pre-trained on a large dataset for a general task (e.g., a CNN trained on image recognition) is adapted for a new, specific task (e.g., antenna performance prediction) with a smaller dataset. In antenna design, this means a DL model trained on a vast repository of existing antenna simulations can be fine-tuned with a relatively small set of new simulation data for a slightly different antenna type or operating environment. This significantly reduces the training data requirement and accelerates the development of new predictive models, enabling faster prototyping and exploration of novel designs without the need to build a comprehensive dataset from scratch for every new antenna concept [51].

3.3. Evolutionary and Natural Computing Algorithms

EAs and broader natural computing paradigms constitute a robust class of metaheuristic optimization techniques inspired by biological evolution and swarm intelligence. Unlike deterministic

gradient-based methods, which are prone to entrapment in local minima, these stochastic algorithms do not require derivative information. Consequently, they are exceptionally well-suited for the complex, discontinuous, and multimodal objective functions frequently encountered in high-dimensional antenna design spaces.

GAs operate on a population of potential solutions (antennas represented by a set of parameters or a binary string encoding geometry). Through iterative application of genetic operators (selection, crossover, mutation), the population "evolves" over generations. Designs with better performance (higher fitness) are more likely to survive and pass on their "genes," leading to a gradual improvement towards optimal solutions. GAs are highly effective for global optimization and exploring vast, irregular design spaces. PSO is another population-based metaheuristic inspired by the social behavior of bird flocking or fish schooling. Each "particle" in the swarm represents a potential solution in the search space. Particles move through the search space, adjusting their trajectories based on their own best-found position (personal best) and the best-found position of the entire swarm (global best). This collective intelligence allows the swarm to efficiently converge towards optimal regions. PSO is often simpler to implement than GAs and can be very effective for continuous optimization problems in antenna design [52].

Figure 3 Flowchart of the Particle Swarm Optimization (PSO) algorithm. The process highlights the iterative mechanism where particles adjust their trajectories in the search space guided by personal best (P_{best}) and global best (G_{best}) values to converge toward the global optimum.

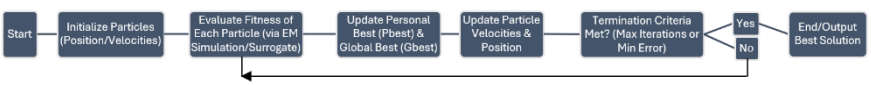

The iterative operational workflow of the PSO algorithm is detailed in the flowchart presented in Fig. 3. In each iteration, the particles update their velocities and positions based on the best solutions they and the swarm have found historically. This cycle continues until a termination criterion is met. The synergistic integration of EAs with Machine Learning forms powerful "Hybrid AI" architectures, often referred to in literature as Surrogate-Assisted Evolutionary Algorithms (SAEAs). In this framework, an EA serves as the primary global optimizer; however, instead of evaluating every candidate design via a computationally expensive full-wave EM simulator, the algorithm queries a high-speed ML/DL surrogate model. This strategy dramatically accelerates the optimization process, enabling the exploration of massive design spaces within practical timeframes. Furthermore, advanced hybrid strategies employ ML to intelligently guide the evolutionary operators (e.g., adaptive mutation), making the search process significantly more directed and efficient.

Designing Multiple-Input Multiple-Output (MIMO) antennas for 5G and emerging 6G systems poses significant challenges. These challenges stem from the necessity of having multiple radiating elements in close proximity. This requires careful management of mutual coupling, ensuring high isolation, and maintaining radiation efficiency and compact form factors. PSO is a highly effective algorithm for optimizing such complex, multi-objective problems. For instance, PSO can simultaneously optimize the placement, orientation, and geometric parameters of multiple antenna elements within an array. The fitness function for each "particle" (a specific MIMO antenna configuration) would typically include objectives like minimizing correlation coefficients, maximizing channel capacity, achieving desired radiation patterns for beamforming, and maintaining acceptable impedance matching across multiple ports. By leveraging PSO, engineers can efficiently

explore the vast design landscape of MIMO arrays, leading to compact, high-performance solutions crucial for the next generation of wireless communication [53,54].

4. Artificial Intelligence in Antenna Manufacturing Processes

While the previous chapters focused on the design and simulation phases, the physical realization of antennas involves distinct challenges related to precision, material properties, and production consistency. The integration of AI into manufacturing, often referred to as Industry 4.0, is revolutionizing how antennas are fabricated. This chapter explores the application of AI in antenna manufacturing, specifically focusing on additive manufacturing optimization, material selection, defect prediction, and automated quality control [55].

Additive manufacturing (3D printing) has gained significant traction in antenna engineering due to its ability to fabricate complex, non-planar geometries that are difficult to achieve with subtractive methods. However, deviations during the printing process can severely impact EM performance. AI algorithms are increasingly employed to enhance the fidelity of 3D-printed antennas. ML models can be trained to optimize slicing parameters (e.g., layer height, infill density, and print speed) based on the specific EM requirements of the antenna. Furthermore, AI-driven geometric compensation techniques are used to predict and counteract thermal deformations or shrinkage that occur during the printing process. By pre-distorting the digital model (CAD), the AI ensures that the final physical prototype matches the intended design with high precision, thereby maintaining the desired resonant frequency and radiation patterns [56].

The performance of an antenna is intrinsically linked to the EM properties of the materials used, particularly the substrate's permittivity and loss tangent. In traditional manufacturing, material

selection is often limited to commercially available standard substrates. AI facilitates a more nuanced approach through the optimization of composite materials and metamaterials. Data-driven approaches allow engineers to predict the effective EM properties of composite mixtures before fabrication. For instance, DL models can analyze the micro-structure of a proposed material mixture and accurately predict its dielectric constant. This capability enables the "inverse design" of materials, where the AI recommends a specific material composition and fabrication parameter set to achieve a target permittivity required for a specific antenna application, significantly reducing the trial-and-error phase in material engineering [57].

In mass production scenarios, equipment failure or process drift can lead to defective antenna batches, resulting in substantial financial loss. AI-powered predictive maintenance and defect prediction systems are critical in mitigating these risks. By leveraging data from sensors embedded in manufacturing equipment (e.g., temperature sensors on extruders, vibration sensors on CNC milling machines), ML algorithms can detect subtle anomalies that precede a failure. Time-series analysis techniques, such as Long Short-Term Memory (LSTM) networks, process this sensor data to forecast potential manufacturing deviations. If the system predicts that a machine's calibration is drifting beyond an acceptable tolerance, which could lead to etching errors in PCBs or structural flaws in 3D prints, it can alert operators or automatically adjust process parameters in real-time to prevent the defect, ensuring consistent production quality [58].

Post-manufacturing inspection is the final gatekeeper of quality. Traditional manual inspection is slow and prone to human error, while rule-based automated optical inspection (AOI) systems often struggle with complex antenna geometries. AI, particularly Computer Vision powered by CNNs, has transformed quality

control. AI-based inspection systems can analyze high-resolution images or X-ray scans of manufactured antennas to detect microscopic defects such as micro-cracks in solder joints, discontinuities in conductive traces, or surface roughness on waveguide components. Unlike traditional methods, these deep learning models can generalize to identify novel defect types they were not explicitly programmed to find. This automated, high-speed verification ensures that only antennas meeting stringent performance standards proceed to the assembly stage, thereby enhancing the overall reliability of wireless communication systems [59].

5. Challenges and Future Perspectives

The integration of AI into antenna engineering has undeniably precipitated a paradigm shift, unlocking unprecedented capabilities in design optimization, simulation acceleration, and manufacturing precision. However, notwithstanding the promising results detailed in preceding chapters, significant hurdles remain that impede the ubiquitous industrial adoption of these technologies. Furthermore, as wireless communication standards evolve toward 6G and Terahertz (THz) frequencies, the role of AI is projected to expand from offline design optimization to real-time, adaptive antenna control. This section critically examines existing bottlenecks and delineates the trends poised to shape the future of intelligent antenna systems.

5.1. Current Challenges in AI-Driven Antenna Engineering

While AI models have demonstrated superior efficacy in specific case studies, their robust deployment in general-purpose antenna engineering confronts obstacles regarding data availability, computational overhead, and model interpretability.

One of the most pervasive challenges in applying AI to EM s is the lack of large-scale, open-source, and standardized datasets.

Unlike fields such as Computer Vision or Natural Language Processing, which benefit from massive repositories like ImageNet, the antenna community relies heavily on synthetic data generated via simulations. Generating "ground truth" data using high-fidelity full-wave EM solvers is computationally expensive and time-consuming. Consequently, many studies rely on small, problem-specific datasets. This limits the reproducibility of results and hinders the development of foundation models capable of understanding generalized electromagnetic (EM) phenomena. Without a unified benchmark dataset, researchers must regenerate data for every new design problem, creating a significant barrier to entry and slowing the field's collective progress [60,61].

Although trained AI models (surrogates) offer rapid inference times, the upfront computational cost of training these models can be substantial. Creating a robust surrogate model often requires thousands of full-wave simulations to populate the design space adequately. For electrically large structures or massive arrays intended for 5G/6G applications, a single data point can take hours to simulate. When combined with the hardware requirements for training DNNs or GANs, which necessitate high-performance GPUs, the total energy and time investment can sometimes approach or exceed that of traditional optimization methods for simpler problems. The "curse of dimensionality" remains a critical issue; as the number of design variables increases, the amount of data required to train an accurate model grows exponentially, challenging the feasibility of AI for highly complex antenna topologies [62,63].

A critical limitation of current data-driven models is their poor generalization capability. A neural network trained to optimize a microstrip patch antenna typically fails completely if applied to a horn antenna or a dielectric resonator antenna. Most AI models in literature are "topology-specific," meaning they learn the statistical correlations of a fixed geometry but do not grasp the underlying

Maxwell’s equations. This lack of physical intuition often leads to the "black box" problem, where the model might predict physically impossible results (e.g., efficiencies greater than 100% or negative resistance) when queried outside its training domain. Ensuring the trustworthiness of AI predictions is paramount; without rigorous validation or physics-informed constraints (such as PINNs), engineers may hesitate to rely on AI for mission-critical aerospace or defense applications.

5.2. Future Trends: The Road to 6G and Beyond

Looking forward, the convergence of EMs and artificial intelligence is poised to deepen. The focus is shifting from using AI merely as a design tool to embedding it as the "brain" of the communication hardware itself.

The transition to 6G networks will utilize the sub-THz and THz spectrums to achieve data rates exceeding 1 Tbps. At these frequencies, propagation losses are severe, requiring ultra-massive MIMO (um-MIMO) arrays with hundreds or thousands of elements to maintain connectivity via high-gain beamforming. Traditional channel estimation and beam management techniques are too slow to handle the high mobility and dynamic blockage characteristic of these frequencies. Future antenna systems will employ AI-native architectures where deep learning algorithms predict channel state information (CSI) and optimize beamforming weights in real-time [64]. These "cognitive antennas" can sense their environment, predict user movement, and proactively adjust their radiation patterns to ensure uninterrupted connectivity. This effectively realizes the concept of smart radio environments [65].

The future of antenna engineering lies in "Generative Design" and autonomous synthesis. Moving beyond simple parameter optimization, future AI systems will function as end-to-end designers. An engineer will simply input high-level

specifications (e.g., "design a dual-band antenna for a wearable device with X gain and Y size constraints"), and the AI, leveraging GANs or RL, will autonomously evolve novel topologies that no human engineer would intuitively conceive. These systems will likely integrate multi-physics simulations to optimize EM performance, thermal dissipation, and mechanical structural integrity simultaneously, thereby streamlining the entire R&D lifecycle from concept to fabrication.

To meet the ultra-low latency requirements (<1 ms) of future applications like autonomous driving and remote surgery, antenna control intelligence must move from the cloud to the extreme edge. This involves implementing lightweight AI models directly on the Field Programmable Gate Arrays (FPGAs) or Application-Specific Integrated Circuits (ASICs) embedded behind the antenna array. "Edge AI" will enable reconfigurable intelligent surfaces (RIS) and phased arrays to adapt to changing interference environments in microseconds. By processing data locally, these smart antennas will reduce the signaling overhead on the network and enable instantaneous self-calibration and fault correction, ensuring the resilience required for next-generation wireless infrastructure [66].

Conclusion

This chapter has provided a comprehensive exploration of the transformative impact of AI on the entire lifecycle of antenna engineering, ranging from initial conceptualization and simulation to physical manufacturing and quality control. The integration of AI is not merely an incremental improvement but represents a fundamental paradigm shift, moving the field from heuristic, trial-and-error methodologies toward data-driven, automated, and intelligent workflows. Summary of Approaches Discussed Throughout the chapter, we have examined a diverse array of AI methodologies tailored for EM problems. We highlighted how ML

algorithms, such as SVMs and Random Forests, serve as powerful tools for parameter estimation and regression. We explored the capabilities of DL, particularly CNNs for predicting radiation patterns from geometric images, and GANs for the inverse design of novel antenna topologies. Furthermore, the role of EAs like GAs and PSO in navigating complex, multi-objective design spaces was detailed. Finally, the extension of AI into the manufacturing domain was discussed, demonstrating its utility in optimizing 3D printing parameters, designing metamaterials, and automating defect detection via computer vision. Contributions of AI to Antenna Engineering The contributions of AI to antenna engineering, as detailed in this work, can be categorized into three primary pillars:

Efficiency and Speed: The most immediate impact is the drastic reduction in computational time. Surrogate model-assisted optimization has proven capable of replacing computationally expensive full-wave EM simulations with rapid inferences, accelerating design cycles from weeks to hours.

Handling Complexity: AI empowers engineers to address problems of high dimensionality and non-linearity that are intractable for traditional analytical methods. This includes the design of complex metasurfaces, large-scale phased arrays, and multi-band antennas where mutual coupling effects are significant.

Precision and Reliability: In the manufacturing phase, AI-driven process control ensures that the physical realization of the antenna matches the simulated design with high fidelity, minimizing waste and ensuring consistent performance in mass production.

Recommendations for Future Research To fully realize the potential of AI in EMs and overcome the remaining challenges, future research efforts can focus on the following key areas:

Development of Standardized Open Datasets: The community must collaborate to establish large-scale, open-access

benchmark datasets for various antenna types. This will facilitate fair comparison of AI models and accelerate the development of "foundation models" for EMs.

Physics-Informed AI Architectures: Future work should prioritize "Physics-Informed Neural Networks" (PINNs) over purely data-driven "black box" models. Incorporating Maxwell's equations directly into the loss functions of neural networks will improve model generalization and ensure physical consistency, even with limited training data.

Real-Time Adaptive Systems for 6G: Research should expand beyond static design optimization to dynamic, real-time control. Developing lightweight AI algorithms capable of running on edge devices is crucial for enabling the cognitive, self-adaptive antenna systems required for 6G and THz communications.

Interdisciplinary Collaboration: Finally, fostering closer collaboration between EM engineers, computer scientists, and material scientists will be essential to solve the multi-physics challenges of future intelligent wireless systems.

Ultimately, the convergence of artificial intelligence and EMs heralds a new era of innovation where the boundaries of physical design are continually expanded. As these intelligent technologies mature, they will not replace but rather augment human engineers, serving as indispensable tools to conceptualize and realize the complex wireless systems of tomorrow. Embracing this data-driven evolution is, therefore, not merely an option but a strategic necessity for unlocking the full potential of future global connectivity.

References

[1] A.E. Çetin, M. Turkmen, S. Aksu, H. Altug, Nanoparticle-based metamaterials as multiband plasmonic resonator antennas,

IEEE Trans Nanotechnol 11 (2012) 208–212. https://doi.org/10.1109/TNANO.2011.2174160.

[2] C.A. Balanis, Antenna Theory Analysis and Design fourth edition, Universitas Nusantara PGRI Kediri 01 (2017).

[3] K. Delihacıoğlu, M. Karaaslan, E. Tetik, E. Ünal, F. Dinçer, F. Karadağ, Low profile antenna radiation enhancement with novel electromagnetic band gap structures, IET Microwaves, Antennas & Propagation 7 (2013) 215–221. https://doi.org/10.1049/iet-map.2012.0545.

[4] G. Geetharamani, T. Aathmanesan, Design of Metamaterial Antenna for 2.4 GHz WiFi Applications, Wirel Pers Commun 113 (2020). https://doi.org/10.1007/s11277-020-07324-z.

[5] S. Chaudhary, A. Kansal, Compact high gain 28, 38 GHz antenna for 5G communication, International Journal of Electronics 110 (2023). https://doi.org/10.1080/00207217.2022.2068201.

[6] C. Loss, R. Gonçalves, C. Lopes, P. Pinho, R. Salvado, Smart Coat with a Fully-Embedded Textile Antenna for IoT Applications, Sensors 16 (2016). https://doi.org/10.3390/s16060938.

[7] J.D. Kraus, R.J. Marhefka, Antennas for all applications, Antennas for All Applications, by Kraus, John Daniel; Marhefka, Ronald J. New York: McGraw-Hill, C2002. 1 (2002).

[8] E. Tetik, G.D. Tetik, The effect of a metamaterial-based wearable microstrip patch antenna on the human body, Can J Phys 96 (2017) 796–800. https://doi.org/10.1139/cjp-2017-0755.

[9] R. Wang, K. Klionovski, A. Shamim, Theory and Design of a 3-D Antenna with Wideband Radiation Isotropy, IEEE Trans Antennas Propag 72 (2024). https://doi.org/10.1109/TAP.2023.3330013.

[10] F.A. Galleto, A.D.M. Africa, A.J.A. Abello, J.M.B. Lalusin, Development of a novel optimization algorithm for a microstrip patch antenna array, Indonesian Journal of Electrical Engineering and Computer Science 33 (2024). https://doi.org/10.11591/ijeecs.v33.i1.pp126-134.

[11] S. Saleh, N. Timmons, J. Morrison, W. Ismail, Compact linearly polarized 5G Vivaldi non-uniform slot filtering antenna, Ain Shams Engineering Journal 15 (2024). https://doi.org/10.1016/j.asej.2023.102364.

[12] C. Han, Y. Chen, L. Yan, Z. Chen, L. Dai, Cross Far- and Near-Field Wireless Communications in Terahertz Ultra-Large Antenna Array Systems, IEEE Wirel Commun 31 (2024). https://doi.org/10.1109/MWC.003.2300004.

[13] H. Paşalıoğlu, L. Wang, M. Bakır, L.C. Paul, E. Tetik, M. Karaaslan, A reconfigurable array and MIMO antenna for 18 GHz and 28/38 GHz applications, Measurement 257 (2026) 118660. https://doi.org/https://doi.org/10.1016/j.measurement.2025.118660.

[14] C. Du, X. Li, S. Zhong, Compact Liquid Crystal Polymer-Based Tri-Band Flexible Antenna for WLAN/WiMAX/5G Applications, IEEE Access 13 (2025). https://doi.org/10.1109/ACCESS.2019.2941212.

[15] Y. Zhou, T. Jiang, H. Li, F. Chen, A 5G MIMO Multiband Low-Profile Antenna Design for Automotive Shark-Fin Systems, IEEE Antennas Wirel Propag Lett 23 (2024). https://doi.org/10.1109/LAWP.2024.3363221.

[16] A. Sabban, Novel Meta-Fractal Wearable Sensors and Antennas for Medical, Communication, 5G, and IoT Applications, Fractal and Fractional 8 (2024). https://doi.org/10.3390/fractalfract8020100.

[17] M. Ashraful Haque, M. Afzalur Rahman, S. Salem Al-Bawri, K. Aljaloud, N. Singh Sawaran Singh, D. Saha, E. Eiyda Hussin, W.M. Abdulkawi, M.A. Zakariya, Machine Learning-Based Approach for bandwidth and frequency Prediction for N77 band 5G Antenna, Phys Scr 99 (2024). https://doi.org/10.1088/1402-4896/ad1d40.

[18] J.-M. Jin, The Finite Element Method in Electromagnetics, 3rd edition, J Chem Inf Model (2014).

[19] A. Taflove, S.C. Hagness, Computational Electrodynamics: The Finite-Difference Time-Domain Method, Third Edition, 2005.

[20] H.M. El Misilmani, T. Naous, S.K. Al Khatib, A review on the design and optimization of antennas using machine learning algorithms and techniques, International Journal of RF and Microwave Computer-Aided Engineering 30 (2020). https://doi.org/10.1002/mmce.22356.

[21] S.K. Goudos, C. Kalialakis, R. Mittra, Evolutionary algorithms applied to antennas and propagation: A review of state of the art, Int J Antennas Propag 2016 (2016). https://doi.org/10.1155/2016/1010459.

[22] S. Koziel, S. Ogurtsov, Antenna Design by Simulation-Driven Optimization, 2014.

[23] Y. LeCun, G. Hinton, Y. Bengio, Deep learning (2015), Y. LeCun, Y. Bengio and G. Hinton, Nature 521 (2015).

[24] C. Jiang, H. Zhang, Y. Ren, Z. Han, K.C. Chen, L. Hanzo, Machine Learning Paradigms for Next-Generation Wireless Networks, IEEE Wirel Commun 24 (2017). https://doi.org/10.1109/MWC.2016.1500356WC.

[25] T. O'Shea, J. Hoydis, An Introduction to Deep Learning for the Physical Layer, in: IEEE Trans Cogn Commun Netw, 2017. https://doi.org/10.1109/TCCN.2017.2758370.

[26] T. Wuest, D. Weimer, C. Irgens, K.D. Thoben, Machine learning in manufacturing: Advantages, challenges, and applications, Prod Manuf Res 4 (2016). https://doi.org/10.1080/21693277.2016.1192517.

[27] J. Wang, Y. Ma, L. Zhang, R.X. Gao, D. Wu, Deep learning for smart manufacturing: Methods and applications, J Manuf Syst 48 (2018). https://doi.org/10.1016/j.jmsy.2018.01.003.

[28] Q. Wu, Y. Cao, H. Wang, W. Hong, Machine-learning-assisted optimization and its application to antenna designs: Opportunities and challenges, China Communications 17 (2020). https://doi.org/10.23919/JCC.2020.04.014.

[29] P. Ranjan, S. Yadav, H. Gupta, A. Bage, Design and Development of Machine Learning Assisted Cylindrical Dielectric Resonator Antenna, Evergreen 10 (2023). https://doi.org/10.5109/6781085.

[30] T.S. Rappaport, Y. Xing, O. Kanhere, S. Ju, A. Madanayake, S. Mandal, A. Alkhateeb, G.C. Trichopoulos, Wireless communications and applications above 100 GHz: Opportunities and challenges for 6g and beyond, IEEE Access 7 (2019). https://doi.org/10.1109/ACCESS.2019.2921522.

[31] G.S. Hornby, A. Globus, D.S. Linden, J.D. Lohn, Automated antenna design with evolutionary algorithms, in: Collection of Technical Papers - Space 2006 Conference, 2006. https://doi.org/10.2514/6.2006-7242.

[32] S. Koziel, A. Pietrenko-Dabrowska, S. Szczepanski, Multi-objective artificial-intelligence-based parameter tuning of antennas

using variable-fidelity machine learning, Sci Rep 15 (2025) 21693. https://doi.org/10.1038/s41598-025-05657-y.

[33] P. Liao, X. Wang, L. An, S. Mao, T. Zhao, C. Yang, TFSemantic: A Time–Frequency Semantic GAN Framework for Imbalanced Classification Using Radio Signals, ACM Trans Sens Netw 20 (2024). https://doi.org/10.1145/3614096.

[34] S. Sasmaz Karacan, E. Tetik, Machine Learning Based Microstrip Patch Antenna Design for Lung Cancer Detection, in: International Congress on Advanced Scientific Studies and Interdisciplinary Research, 2024.

[35] Y. Rahmat-Samii, E. Michielssen, Electromagnetic Optimization by Genetic Algorithms, Microw J (Int Ed) 42 (1999).

[36] J. Robinson, Y. Rahmat-Samii, Particle swarm optimization in electromagnetics, IEEE Trans Antennas Propag 52 (2004). https://doi.org/10.1109/TAP.2004.823969.

[37] S. Koziel, N. Çalık, P. Mahouti, M.A. Belen, Low-Cost and Highly Accurate Behavioral Modeling of Antenna Structures by Means of Knowledge-Based Domain-Constrained Deep Learning Surrogates, IEEE Trans Antennas Propag 71 (2023) 105–118. https://doi.org/10.1109/TAP.2022.3216064.

[38] B. Liu, H. Aliakbarian, Z. Ma, G.A.E. Vandenbosch, G. Gielen, P. Excell, An efficient method for antenna design optimization based on evolutionary computation and machine learning techniques, IEEE Trans Antennas Propag 62 (2014). https://doi.org/10.1109/TAP.2013.2283605.

[39] D.B. Davidson, computational electromagnetics for RF and microwave engineering, 2005. https://doi.org/10.1017/CBO9780511611575.

[40] J.E. Rayas-Sanchez, EM-based optimization of microwave circuits using artificial neural networks: the state-of-the-art, IEEE Trans Microw Theory Tech 52 (2004) 420–435. https://doi.org/10.1109/TMTT.2003.820897.

[41] C.G. Christodoulou, Y. Tawk, S.A. Lane, S.R. Erwin, Reconfigurable antennas for wireless and space applications, in: Proceedings of the IEEE, 2012. https://doi.org/10.1109/JPROC.2012.2188249.

[42] M. Raissi, P. Perdikaris, G.E. Karniadakis, Physics-informed neural networks: A deep learning framework for solving forward and inverse problems involving nonlinear partial differential equations, J Comput Phys 378 (2019) 686–707. https://doi.org/https://doi.org/10.1016/j.jcp.2018.10.045.

[43] K.S. Muttair, O.A. Shareef, H.B. Taher, Machine Learning Based on Antennas Modeling for 5G and 6G Communication Systems: A Systematic Review, International Journal of Communication Systems 38 (2025) e70105. https://doi.org/https://doi.org/10.1002/dac.70105.

[44] M.O. Akinsolu, K.K. Mistry, B. Liu, P.I. Lazaridis, P. Excell, Machine Learning-assisted Antenna Design optimization: A Review and the State-of-the-art, in: 14th European Conference on Antennas and Propagation, EuCAP 2020, 2020. https://doi.org/10.23919/EuCAP48036.2020.9135936.

[45] E. Avşar Aydin, M. Kaya Keleş, UWB Rectangular Microstrip Patch Antenna Design in Matching Liquid and Evaluating the Classification Accuracy in Data Mining Using Random Forest Algorithm for Breast Cancer Detection with Microwave, Journal of Electrical Engineering and Technology 14 (2019). https://doi.org/10.1007/s42835-019-00205-x.

[46] S. Karacan Sasmaz, E. Tetik, The Design of a Metamaterial-Inspired Machine Learning-Based Patch Antenna for Brain Cancer Detection, in: 2nd International Canadian Scientific Research Congress, Toronto, 2024.

[47] Q. Wu, W. Chen, C. Yu, H. Wang, W. Hong, Machine-Learning-Assisted Optimization for Antenna Geometry Design, IEEE Trans Antennas Propag 72 (2024) 2083–2095. https://doi.org/10.1109/TAP.2023.3346493.

[48] N. Chhaule, C. Koley, S. Mandal, A. Onen, T.S. Ustun, A Comprehensive Review on Conventional and Machine Learning-Assisted Design of 5G Microstrip Patch Antenna, Electronics (Basel) 13 (2024). https://doi.org/10.3390/electronics13193819.

[49] A. Tamminen, J. Zheng, S.-V. Pälli, J. Ala-Laurinaho, Z.D. Taylor, Antenna radiation pattern predictions with machine learning, in: 2021 IEEE Conference on Antenna Measurements & Applications (CAMA), 2021: pp. 434–437. https://doi.org/10.1109/CAMA49227.2021.9703477.

[50] D. Ustun, A. Toktas, A. Akdagli, Deep neural network–based soft computing the resonant frequency of E–shaped patch antennas, AEU - International Journal of Electronics and Communications 102 (2019) 54–61. https://doi.org/https://doi.org/10.1016/j.aeue.2019.02.011.

[51] A. Gupta, U.K. Khankhoje, Transfer Learning Based Rapid Design of Frequency and Dielectric Agile Antennas, IEEE J Multiscale Multiphys Comput Tech 10 (2025) 47–57. https://doi.org/10.1109/JMMCT.2024.3509773.

[52] J.M. Johnson, Y. Rahmat-Samii, Genetic algorithms in engineering electromagnetics, IEEE Antennas Propag Mag 39 (1997). https://doi.org/10.1109/74.632992.

[53] A.D. Boursianis, S.K. Goudos, T. V Yioultsis, K. Siakavara, P. Rocca, MIMO Antenna Design for 5G Communication Systems Using Salp Swarm Algorithm, in: 2020 International Workshop on Antenna Technology (IWAT), 2020: pp. 1–3. https://doi.org/10.1109/iWAT48004.2020.1570618331.

[54] S.F. Bin Faruquee, H. Bhuiyan, Md.S. Alam, S. Islam, K. Ali, Swarm intelligence driven inverse design of slot patterns for sub-6 GHz 5G MIMO antennas in virtual reality applications, Engineering Science and Technology, an International Journal 64 (2025) 102026. https://doi.org/https://doi.org/10.1016/j.jestch.2025.102026.

[55] J. Lee, H.A. Kao, S. Yang, Service innovation and smart analytics for Industry 4.0 and big data environment, in: Procedia CIRP, 2014. https://doi.org/10.1016/j.procir.2014.02.001.

[56] C. Wang, X.P. Tan, S.B. Tor, C.S. Lim, Machine learning in additive manufacturing: State-of-the-art and perspectives, Addit Manuf 36 (2020) 101538. https://doi.org/10.1016/J.ADDMA.2020.101538.

[57] W. Ma, F. Cheng, Y. Liu, Deep-Learning-Enabled On-Demand Design of Chiral Metamaterials, ACS Nano 12 (2018). https://doi.org/10.1021/acsnano.8b03569.

[58] R. Zhao, R. Yan, Z. Chen, K. Mao, P. Wang, R.X. Gao, Deep learning and its applications to machine health monitoring, Mech Syst Signal Process 115 (2019). https://doi.org/10.1016/j.ymssp.2018.05.050.

[59] A. Saberironaghi, J. Ren, M. El-Gindy, Defect Detection Methods for Industrial Products Using Deep Learning Techniques: A Review, Algorithms 16 (2023). https://doi.org/10.3390/a16020095.

[60] Z. Zhou, Z. Wei, J. Ren, Y. Yin, G.F. Pedersen, M. Shen, Two-Order Deep Learning for Generalized Synthesis of Radiation Patterns for Antenna Arrays, IEEE Transactions on Artificial Intelligence 4 (2023) 1359–1368. https://doi.org/10.1109/TAI.2022.3192505.

[61] P.A. Gajbhiye, S.P. Singh, M.K. Sharma, A comprehensive review of AI and machine learning techniques in antenna design optimization and measurement, Discover Electronics 2 (2025) 46. https://doi.org/10.1007/s44291-025-00084-9.

[62] J. Sun, Y. Tian, Z. Zhu, BNN-LSTM-DE Surrogate Model–Assisted Antenna Optimization Method Based on Data Selection, International Journal of RF and Microwave Computer-Aided Engineering 2024 (2024) 6622761. https://doi.org/https://doi.org/10.1155/mmce/6622761.

[63] S. Koziel, A. Pietrenko-Dabrowska, L. Leifsson, Antenna optimization using machine learning with reduced-dimensionality surrogates, Sci Rep 14 (2024) 21567. https://doi.org/10.1038/s41598-024-72478-w.

[64] M. Di Renzo, A. Zappone, M. Debbah, M.S. Alouini, C. Yuen, J. De Rosny, S. Tretyakov, Smart Radio Environments Empowered by Reconfigurable Intelligent Surfaces: How It Works, State of Research, and the Road Ahead, IEEE Journal on Selected Areas in Communications 38 (2020). https://doi.org/10.1109/JSAC.2020.3007211.

[65] K.B. Letaief, W. Chen, Y. Shi, J. Zhang, Y.J.A. Zhang, The Roadmap to 6G: AI Empowered Wireless Networks, IEEE Communications Magazine 57 (2019). https://doi.org/10.1109/MCOM.2019.1900271.

[66] J. Park, S. Samarakoon, M. Bennis, M. Debbah, Wireless Network Intelligence at the Edge, Proceedings of the IEEE 107 (2019). https://doi.org/10.1109/JPROC.2019.2941458.

CHAPTER 4

COMPARATIVE EVALUATION OF GAMMA-RAY SHIELDING PROPERTIES OF IRON-BASED MINERALS USING ATTENUATION AND THICKNESS PARAMETERS

Kadir GÜNOĞLU [1]

1. Introduction

With the rapid advancement of modern technology, applications involving high-energy photons have expanded across a broad spectrum, ranging from medical technologies and energy systems to industrial quality control processes and advanced research infrastructures. Ensuring safe working conditions in such applications, controlling radiation exposure, and maintaining structural integrity have made the development of effective radiation shielding materials a critical requirement. In this context, growing attention has been directed toward materials that not only exhibit high attenuation capability but are also environmentally benign, economically viable, and structurally sustainable (Mann, et al., 2016; Singh, et al., 2018)

[1] Doç. Dr., Isparta Uygulamalı Bilimler Üniversitesi, Teknik Bilimler Meslek Yüksekokulu, kadirgunoglu@isparta.edu.tr, ORCID: 0000-0002-9008-9162.

Conventional shielding materials such as lead and concrete provide effective protection due to their high densities; however, they suffer from several significant drawbacks, including toxicity, excessive weight, limited workability, and long-term environmental concerns. These limitations necessitate the exploration of alternative materials, particularly for next-generation lightweight, modular, and multifunctional shielding systems. Accordingly, natural minerals and metal oxides have emerged as promising candidates owing to their low cost, wide availability, and chemical stability (Azeez, 2019; Abouhaswa, 2020; Gunoglu, 2024).

Iron-based minerals possess considerable potential for radiation shielding applications due to their relatively high atomic numbers and the presence of elements that actively participate in photon–matter interactions. Iron oxides and iron-containing minerals such as magnetite (Fe_3O_4), hematite (Fe_2O_3), limonite ($FeO(OH)\cdot nH_2O$), siderite ($FeCO_3$), and goethite (α-FeO(OH)) exhibit distinct oxidation states, crystal structures, and bonding characteristics. These structural and chemical differences are expected to directly influence their photon energy–dependent attenuation behavior (Kavaz, E., 2019; Gunoglu and Akkurt, I., 2021; Oto, 2025) .

The quantitative assessment of radiation shielding performance is commonly based on key parameters, including the mass attenuation coefficient (MAC), linear attenuation coefficient (LAC), half-value layer (HVL), tenth-value layer (TVL), and mean free path (MFP). While MAC and LAC describe the probability of photon interactions within a material, HVL, TVL, and MFP provide practical guidance for determining the required shielding thickness in engineering applications. Photoelectric absorption at low energies, Compton scattering at intermediate energies, and pair formation at high energies are the primary interaction processes linked to the substantial dependency of these characteristics on photon energy.

Although experimental methods offer high accuracy, comprehensive experimental investigations for every material are not always feasible due to radiation safety requirements, cost, and time constraints. Consequently, theoretical and computational approaches have become effective tools for the preliminary evaluation of potential shielding materials. The PhyX-PSD software is a widely used platform that enables reliable calculation of radiation shielding parameters over a broad photon energy range based on the chemical composition and density of materials (Şakar et al., 2020).

Despite the extensive literature on iron-based synthetic composites, studies that systematically and comparatively examine the radiation shielding properties of natural iron oxide minerals remain limited. In particular, evaluating magnetite, hematite, limonite, siderite, and goethite using a unified theoretical framework is crucial for elucidating the relationship between mineralogical structure and shielding performance.

In this study, the gamma-ray shielding characteristics of magnetite, hematite, limonite, siderite, and goethite minerals were theoretically investigated using the PhyX-PSD program. MAC, LAC, HVL, TVL and MFP parameters were computed over a broad range of photon energies, and the outcomes were compared using dominant photon interaction mechanisms and mineral composition. It is anticipated that the results of this study will further knowledge about the potential of naturally occurring iron oxide minerals for radiation shielding applications.

2. MATERIALS AND METHODS

The decrease in the intensity of ionizing photon radiation, including gamma rays and X-rays, during transmission through a shielding medium is governed by the fundamental mechanisms of photon–matter interaction. These mechanisms primarily involve

photoelectric absorption, Compton scattering, and, at sufficiently high photon energies, pair production. Owing to the probabilistic nature of these interactions, the attenuation of photons follows a statistical behavior and is conventionally modeled using the Beer–Lambert formalism (Bashter, 1997). Within this framework, the relationship between the incident photon intensity I_0 and the emerging intensity I after traversing a homogeneous material of thickness x can be described as follows:

$$I = I_0 e^{-\mu x} \tag{1}$$

where μ denotes the LAC.

The LAC, expressed in units of cm^{-1}, represents the probability of photon attenuation per unit path length within a material. This parameter directly characterizes the rate at which photon interactions occur inside the shielding medium. The magnitude of the LAC is influenced by several factors, including material density, elemental composition, atomic number, and the energy of the incident photons. Larger LAC values correspond to enhanced shielding performance, indicating that photons are attenuated over shorter distances as they traverse the material.

Since MAC characterizes the probability of photon–matter interactions per unit mass, it is considered independent of density and is therefore widely used as a comparative parameter for evaluating the shielding performance of materials with different densities. For composite or multi-component materials, the MAC can be calculated using the weight fractions of the constituent elements based on the additive nature of photon interactions, as follows (Gunoglu et al., 2021):

$$(\mu/\rho)_{composite} = \sum_i w_i \, (\mu/\rho)_i \tag{2}$$

where w_i is the weight fraction of the i_{th} component.

The minimal thickness of a shielding material needed to lower the incident photon intensity to 50% of its initial value is known as the HVL. An engineering-friendly and useful metric of shielding performance is HVL. It can be represented quantitatively as follows and is inversely proportional to the linear attenuation coefficient (Gunoglu, 2024):

$$HVL\left(X_{\frac{1}{2}}, cm\right) = \frac{Ln(2)}{\mu} \tag{3}$$

Lower HVL values indicate that effective radiation shielding can be achieved with thinner material layers.

The TVL represents the thickness of a material needed to attenuate the incident photon intensity to 10% of its initial value. TVL is particularly relevant in applications demanding high levels of radiation protection, such as nuclear facilities and medical radiation environments (Gunoglu, 2024). It is larger than the HVL and is defined as

$$TVL\left(X_{\frac{1}{10}}, cm\right) = \frac{Ln(10)}{\mu} \tag{4}$$

The MFP, which characterizes the average distance a photon travels between subsequent contacts within the material, is another crucial shielding characteristic (Gunoglu, 2024). This value, which is equal to the inverse of the linear attenuation coefficient, represents the stochastic character of photon-matter interactions:

$$MFP\ (\lambda, cm) = \frac{1}{\mu} \tag{5}$$

Smaller MFP values indicate more frequent photon interactions and, consequently, superior shielding performance.

When considered together, these parameters offer a robust and comprehensive evaluation of a material's effectiveness in attenuating gamma radiation. It is widely recognized that increases

in material density and atomic number result in enhanced LAC and MAC values, while concurrently leading to decreases in HVL, TVL, and MFP. This trend underscores the strong potential of composite materials that incorporate high-density and high–atomic-number reinforcing phases for use in advanced radiation shielding systems.

3. RESULTS AND DISCUSSION

In this work, the PhyX-PSD software was used to theoretically predict the fundamental radiation shielding properties of iron oxide minerals, such as magnetite, hematite, limonite, siderite, and goethite. Based on the density and chemical makeup of the materials, this tool determines shielding values for gamma-ray energy between 0.01 and 0.05 MeV. Table 1 summarizes the densities and chemical compositions of the iron oxide minerals under investigation.

Table 1. Chemical formula and density of iron minerals

Minerals	Chemical Formula	Density (g/cm^3)
Magnetite	Fe_3O_4	5,18
Hematite	Fe_2O_3	5,3
Limonite	FeO_3H_3	3,4
Siderite	$FeCO_3$	4,0
Goethite	FeO_2H	4,26

The MAC and LAC values of different iron-based minerals such as magnetite, hematite, limonite, siderite, and goetite, and their variation with photon energy, are given in Figure 1 and Figure 2. These graphs clearly demonstrate both the energy-dependent interaction mechanisms and the effect of mineral type and chemical content differences on shielding behavior.

Figure 1. MAC values for the iron minerals

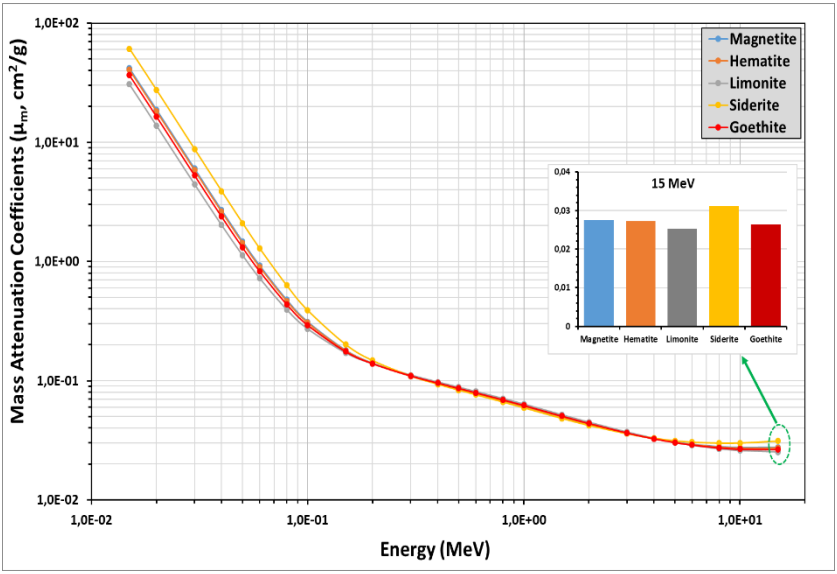

Figure 2. LAC values for the iron minerals

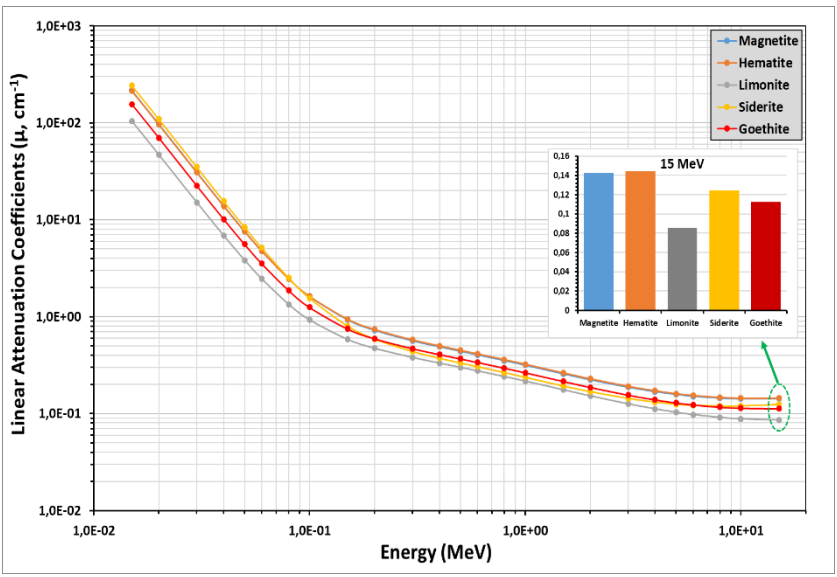

In the low-energy region (approximately 0.01–0.05 MeV), all investigated minerals exhibit relatively high MAC and LAC values.

In this energy range, the photoelectric absorption mechanism is dominant, and its probability strongly depends on the atomic number (Z) of the constituent elements. Minerals with higher iron content and denser phases—particularly siderite and magnetite—display higher attenuation coefficients compared to limonite and goethite. The comparatively elevated MAC and LAC values of siderite can be attributed not only to its iron content but also to its crystal structure and the presence of carbon and oxygen in its composition, which enhance the probability of photon absorption. In contrast, hydrated iron oxide/hydroxide minerals such as limonite and goethite show relatively lower attenuation coefficients in this region due to their bonded water content and lower atomic numbers.

As the photon energy increases into the intermediate-energy region (approximately 0.05–1 MeV), a pronounced decrease in both MAC and LAC values is observed. Within this range, Compton scattering becomes the predominant interaction mechanism, and the interaction probability is governed mainly by electron density rather than atomic number. Consequently, the differences among the various mineral types diminish significantly. The convergence of the attenuation curves reflects the similar electron densities of iron oxide minerals. In this region, magnetite and hematite generally exhibit nearly identical behavior, while limonite and goethite remain at the lower end due to their reduced densities.

In the high-energy region (≈1–15 MeV), MAC values decrease to very low levels and show a more gradual variation with increasing photon energy. Although pair production begins to contribute in this range, its effect remains limited due to the intermediate atomic number characteristics of iron-based minerals. The inset plots corresponding to 15 MeV indicate that the differences among mineral types are minimal; nevertheless, siderite and magnetite retain a slightly superior attenuation capability. For LAC values, the influence of material density becomes more pronounced,

with higher-density minerals—particularly magnetite and hematite—achieving larger LAC values at identical photon energies.

Overall, MAC values are primarily governed by chemical composition and atomic number, whereas LAC values are influenced by these factors in conjunction with material density. Hydrated and relatively porous minerals such as limonite and goethite exhibit lower shielding performance in terms of both parameters. In contrast, dense, iron-rich minerals—including magnetite, hematite, and especially siderite—demonstrate more effective gamma-ray shielding behavior over a wide energy range. These findings clearly indicate that, in the selection of iron oxide–based minerals for radiation shielding applications, not only iron content but also mineral phase, crystal structure, and density must be considered simultaneously.

All three metrics clearly and consistently rise with increasing photon energy for magnetite, hematite, limonite, siderite and goethite when the HVL (Figure 3), TVL (Figure 4), and MFP (Figure 5) graphs are examined.

Figure 3. HVLvalues for the iron minerals

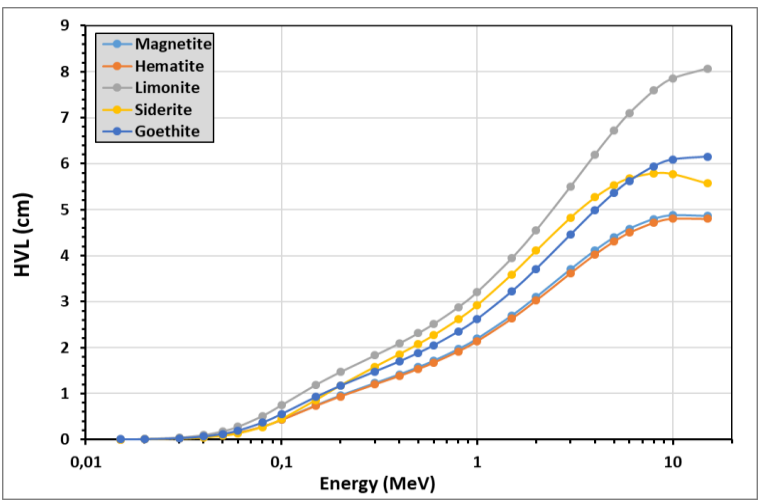

Fikgure 4. TVL values for the iron minerals

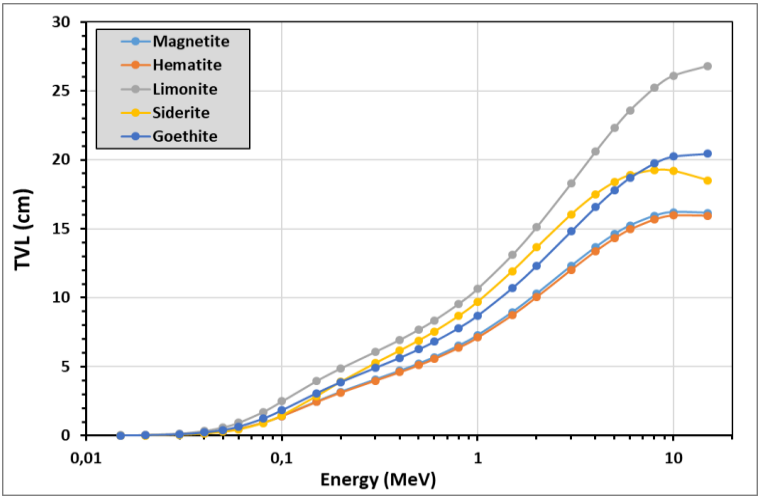

Figure 5. MFP values for the iron minerals

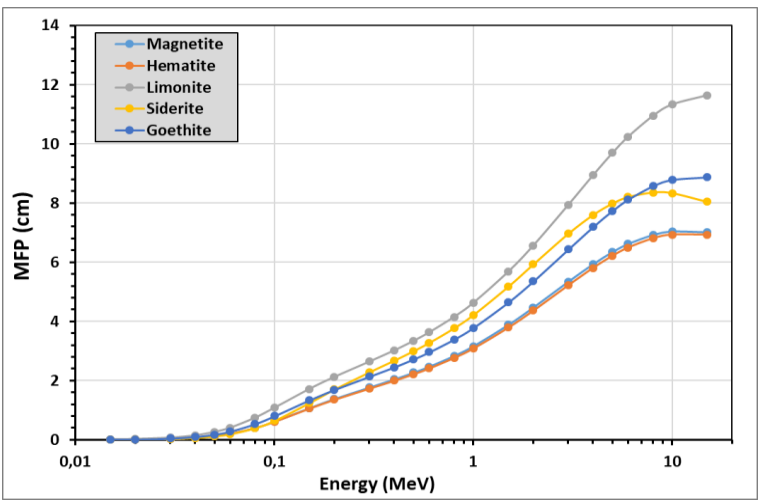

In the low-energy region (≈0.01–0.05 MeV), the HVL, TVL, and MFP values of all investigated minerals are extremely small and approach zero. This behavior is primarily attributed to the dominance of the photoelectric absorption mechanism, which causes photons to be absorbed over very short penetration distances. Within this energy range, magnetite and hematite—characterized by higher

density and atomic number—exhibit the lowest HVL, TVL, and MFP values, indicating superior shielding efficiency. In contrast, limonite and goethite, which possess hydrated structures and comparatively lower densities, require greater shielding thicknesses at the same photon energies.

As the photon energy increases into the intermediate-energy region (≈0.05–1 MeV), a systematic and pronounced rise in HVL, TVL, and MFP values is observed for all minerals. In this range, Compton scattering becomes the dominant interaction mechanism, and the attenuation probability is largely governed by electron density. As a result, although the differences among mineral types diminish, they do not disappear entirely. The plots indicate that limonite reaches the highest HVL, TVL, and MFP values in this region, which can be attributed to its lower density and higher content of structurally bound water. Conversely, siderite and magnetite remain more advantageous by requiring relatively smaller shielding thicknesses.

In the high-energy region (≈1–15 MeV), the increasing trend of HVL, TVL, and MFP values persists; however, the slope of the curves decreases, and the parameters exhibit a more gradual variation with energy. At these energies, photon penetration capability is significantly enhanced, while the contribution of pair production remains limited for iron-based minerals. Notably, the TVL and MFP plots show that limonite attains the highest values, indicating that substantially thicker shielding is necessary to attenuate high-energy gamma rays. Magnetite and hematite, on the other hand, maintain comparatively lower HVL and TVL values even at elevated energies, demonstrating more effective shielding performance.

From a general comparative perspective, the ordering of HVL, TVL, and MFP values closely follows an inverse trend relative to the LAC values. Minerals with higher density and iron content,

such as magnetite and hematite, consistently exhibit smaller HVL, TVL, and MFP values over a wide energy range, whereas limonite and goethite show inferior shielding performance. Siderite demonstrates a balanced behavior, particularly in the intermediate- and high-energy regions, with values comparable to those of magnetite and hematite, suggesting its potential as an alternative shielding material. These results clearly indicate that, when selecting iron oxide–based minerals for gamma-ray shielding applications, energy-dependent performance as well as density–composition relationships must be evaluated simultaneously.

4. CONCLUSION

In this study, the gamma-ray shielding performances of magnetite, hematite, limonite, siderite, and goethite were systematically evaluated over a wide photon energy range by means of mass attenuation coefficient (MAC), linear attenuation coefficient (LAC), half value layer (HVL), tenth value layer (TVL), and mean free path (MFP) parameters. The results clearly demonstrate that photon energy and mineralogical characteristics play a decisive role in determining the attenuation behavior of iron-based minerals.

At low photon energies, where photoelectric absorption dominates, all investigated minerals exhibit high MAC and LAC values and correspondingly low HVL, TVL, and MFP values. In this region, minerals with higher atomic number and compact crystal structures, particularly magnetite and siderite, provide superior shielding efficiency. The relatively lower performance of limonite and goethite is mainly attributed to their hydrated structures and lower effective densities, which reduce the probability of photon interaction.

In the intermediate energy region governed by Compton scattering, attenuation coefficients decrease markedly and the differences between minerals become less pronounced.

Nevertheless, density-dependent parameters such as LAC, HVL, TVL, and MFP still reveal discernible distinctions among the samples. Magnetite and hematite consistently require smaller shielding thicknesses, whereas limonite exhibits the highest HVL, TVL, and MFP values, indicating a weaker shielding capability in this energy range.

At high photon energies, where pair production begins to contribute, the attenuation parameters show a more gradual variation with energy. Although the overall shielding effectiveness of all minerals decreases, magnetite and hematite maintain comparatively lower HVL and TVL values, while limonite remains the least effective material due to its low density and mineralogical composition. Siderite displays an intermediate but stable behavior across medium-to-high energies, suggesting its potential as an alternative shielding material when balanced performance is required.

Overall, the comparative analysis reveals that the gamma-ray shielding efficiency of iron-based minerals is governed not only by iron content but also by mineral phase, density, and structural characteristics. Among the investigated materials, magnetite and hematite emerge as the most effective natural shielding candidates over a broad energy range, whereas limonite and goethite are less favorable, particularly at higher photon energies. These findings provide valuable insight for the selection and optimization of iron-based minerals in radiation shielding applications and can serve as a reference for the development of mineral-reinforced composite shielding materials.

REFERENCES

Abouhaswa, A.S., Al-Buriahi, M.S., Chalermpon, M., Rammah, Y.S., (2020). Influence of ZrO2 on gamma shielding

properties of lead borate glasses. Appl. Phys. A Mater. Sci. Process. 126.

Azeez, M.O., Ahmad, S., Al-Dulaijan, S.U., Maslehuddin, M., Abbas Naqvi, A., (2019). Radiation shielding performance of heavy-weight concrete mixtures. Constr. Build. Mater. 224.

Bashter, I.I., (1997). Calculation of radiation attenuation coefficients for shielding concretes. Ann. Nucl. Energy 24, 1389.

Gunoglu K., (2024). Effect of colemanite mineral on gamma radiation attenuation properties of vinyl ester resin. Journal of Radiation Research and Applied Sciences 17 (2024) 100799, 1-7

Gunoglu K., Akkurt, I., (2021).Radiation shielding properties of concrete containing magnetite. Progress in Nuclear Energy 137, 103776, 1-8

Kavaz, E., (2019). An experimental study on gamma ray shielding features of lithium borate glasses doped with dolomite, hematite and goethite minerals. Radiation Physics and Chemistry 160, 112–123

Mann, H.S., Brar, G.S., Mudahar, G.S., (2016). Gamma-ray shielding effectiveness of novel light-weight clay-flyash bricks. Radiat. Phys. Chem. 127.

Oto, B., Kavaz, E., Madak, Z., Çakar N., (2025). An experimental study on the radiation shielding properties of new type ceramics containing limonite and hematite minerals. Materials Chemistry and Physics 340, 130841, 1-11

Singh, M., Tondon, A., Sandhu, B.S., Singh, B., (2018). Energy dependence of radiation interaction parameters of some organic compounds. Radiat. Phys. Chem. 145.

Şakar, E., Özpolat, Ö.F., Alım, B., Sayyed, M.I., Kurudirek, M., (2020). Phy-X/PSD: development of a user friendly online

software for calculation of parameters relevant to radiation shielding and dosimetry, Radiat. Phys. Chem. 166, 108496

CHAPTER 5

THEORETİCAL ANALYSİS OF THE RADİATİON SHİELDİNG PROPERTİES OF OXİDE-, CARBİDE-, AND NİTRİDE-REİNFORCED Cr–Mo–Nb–Ta–V BASED HİGH-ENTROPY COMPOSİTE MATERİALS USİNG THE WINXCOM, EPIXS, PHY-X/PSD, AND PY-MLBUF SOFTWARE

Rafet YILMAZ[1]
Hamza TUNÇ[2]

INTRODUCTION

Today, radiation is considered one of the most significant physical factors that directly affect human health and environmental safety. In particular, the widespread use of nuclear energy systems and the rapid increase in the number of technological devices used in daily life have led to a rise in radiation exposure, creating a serious area of concern. Long-term or high-

[1] Prof. Dr. Van Yüzüncü Yıl University Department of Physics, Faculty of Science, Orcıd: 000-0003-2734-8763
[2] Öğ. Gör. Dr. Van Yüzüncü Yıl University Muradiye Vocational School, Department of Medical Services and Techniques, Orcıd: 0000-0002-2787-8126

dose exposure to ionizing radiation can cause cellular damage, genetic disorders, and severe health problems such as cancer.

In this context, radiation shielding is defined as a set of protective measures developed to prevent or reduce the exposure of humans and the environment to harmful types of radiation, such as gamma rays, X-rays, and neutrons. Radiation shielding applications play a vital role in many fields, including medical applications (radiology and radiotherapy units), nuclear power plants, industrial facilities, and military operations. The effectiveness of shielding materials varies depending on the type of radiation, its energy, and the duration of exposure.

Ceramics constitute an important class of materials for radiation shielding applications due to their combination of high density, thermal and chemical stability, and mechanical strength. Ceramics doped with heavy metal oxides or rare earth elements, in particular, exhibit high attenuation capacity against gamma and neutron radiation.

In recent years, scientific studies aimed at eliminating or minimizing the harmful effects of radiation have increased significantly. This has led researchers to move beyond traditional shielding materials and focus on developing a new generation of shielding materials that are lighter, more economical, environmentally friendly, and have high radiation absorption capacity. Significant research exists on glass concrete, ceramics, alloys, and high-entropy alloys among these materials.

Glass-based materials have gained significant importance in radiation shielding applications due to their structural homogeneity and high formability in production processes. The study conducted by Kavgacı et al. (2024) comprehensively investigated strontium borate glasses reinforced with ZnO nanoparticles, focusing on their structural, optical, and mechanical

properties, as well as evaluating their radiation shielding effectiveness. The authors reported that oxide doping significantly enhances the radiation shielding performance of the glass system. Rasul et al. (2025) investigated the effect of HfO_2 addition on the structural, thermal, gamma-ray, and neutron shielding properties of boro-tellurite glasses and reported that increasing HfO_2 content significantly enhances radiation shielding performance. Saudi and Gomaa (2019) investigated the effect of Nb_2O_5 addition on the structural and optical properties as well as the fast neutron removal cross section of calcium borate glasses containing Bi^{3+} ions, and reported that Nb_2O_5 incorporation improves the neutron shielding performance of the glasses. Yalcin, Aktas, and Yilmaz (2019) investigated the gamma-ray shielding properties of obsidian glasses doped with cerium oxide (CeO_2) and erbium oxide (Er_2O_3), and reported that oxide doping significantly enhances the radiation attenuation capability of the glass samples.

Concrete is widely used as a radiation shielding material due to its high density, cost-effectiveness, and workability. Onaizi et al. (2024) presented a comprehensive review on radiation-shielding concrete, systematically examining the materials used, their shielding performance, and the effects of radiation on the mechanical and physical properties of concrete. Zorla et al. (2017) investigated the radiation shielding properties of high-performance concrete reinforced with basalt fibers infused with natural and enriched boron, and reported significant improvements in gamma-ray and neutron shielding performance due to boron incorporation.

Ceramics constitute an important class of materials for radiation shielding applications due to their combination of high density, thermal and chemical stability, and mechanical strength. Ceramics doped with heavy

metal oxides or rare earth elements, in particular, exhibit high attenuation capacity against gamma and neutron radiation.Madak et al., (2025) investigated the gamma-ray and neutron shielding performance of $Al_2Si_2O_5(OH)_4$–$KAlSi_3O_8$–SiO_2 ceramics doped with CeO_2 and Er_2O_3, and reported that oxide doping significantly enhances the radiation attenuation capabilities of the ceramic materials.

Alloys are studied as radiation shielding materials due to their superior properties, including mechanical strength, corrosion resistance, and thermal stability. In particular, high-entropy alloys (HEAs), which consist of multiple principal elements in near-equiatomic proportions, exhibit unique microstructural features and enhanced mechanical and thermal performance. These characteristics make HEAs potentially effective materials for gamma and neutron radiation shielding. The composition, density, and phase structure of an alloy are critical parameters that directly influence its radiation attenuation capacity. Sakar (2020) investigated the photon-shielding characteristics and build-up factors of nickel–silver alloys, providing a detailed evaluation of their gamma-ray attenuation performance and highlighting the influence of alloy composition on shielding effectiveness.Wang et al. (2021) developed flexible, low-melting-point radiation shielding materials by incorporating GaInSnPbBi high-entropy alloy inclusions into soft elastomer matrices, and demonstrated that these composites exhibit enhanced gamma-ray shielding performance while maintaining mechanical flexibility.Adamson, Coleman, and Griffiths (2019) critically reviewed irradiation creep and irradiation-induced dimensional changes (growth) in zirconium alloys, evaluating the underlying physical mechanisms, experimental findings, and their implications under nuclear reactor conditions. Alım (2020) conducted a comprehensive study on the radiation shielding characteristics of Tin-Silver, Manganin-R, Hastelloy-B,

Hastelloy-X, and Dilver-P alloys, systematically evaluating their gamma-ray attenuation capabilities and identifying alloys with superior shielding performance.

In this study, the gamma radiation shielding properties of Cr–Mo–Nb–Ta–V-based high-entropy alloys reinforced with oxide (Ta_2O_5), carbide (HfC), and nitride (TiN) phases were theoretically investigated using WinXCOM(Gerward et al.,2004), EpiXS(Hila et al.,2021), Phy-X/PSD(sakar etal., 2020), and Py-MLBUF software. Calculations were performed in the energy range of 0.015–15 MeV, and the fundamental shielding parameters describing the interaction of gamma photons with matter—mass attenuation coefficient (MAC), linear attenuation coefficient (LAC), half-value thickness (HVL), mean free path (MFP), effective atomic number (Z_{eff}), electron density (N_{el}), energy absorption concentration factor (EABF), and exposure concentration factor (EBF) were calculated.

METHOD

The theoretical calculations were carried out using the EpiXS [41], WinXCOM [42], and Phy-X/PSD [43] software packages, which are based on internationally recognized databases and physical models for determining photon–matter interaction parameters. The WinXCOM program calculates mass attenuation coefficients for elements and compounds using the XCOM database developed by NIST. EpiXS provides high-accuracy results by integrating up-to-date cross-section data with advanced theoretical models. Phy-X/PSD is a web-based platform that enables the rapid, consistent, and user-friendly determination of XCOM-based radiation shielding parameters. These software tools yield mutually consistent and comparable results within

the energy range of 0.015–15 MeV, thereby supporting the reliability and validity of the theoretical evaluations performed in this study.

CALCULATİONS

This study examines attenuation processes resulting from the interaction of photons with matter, focusing on both absorption and scattering phenomena, based on Lambert's law. Attenuation due to absorption, in particular, is defined and evaluated within the framework of Beer-Lambert's Law,(Abouhaswa et al.,2025).

$$I = I_0 e^{-\mu t} \tag{1}$$

in this expression, the unit of linear absorption coefficient is μ (cm^{-1}), I_0 represents the initial photon intensity, and I represents the photon intensity after passing through the material. The parameter t corresponds to the material thickness. The mass absorption coefficient (μ/ρ) of a material (or compound) is in cm^2/g.(Mariyappan et al., 2018).

$$(\mu/\rho)_C = \sum w_i (\mu/\rho)_i \tag{2}$$

In this context, (w_i) and (μ/ρ)i denote the weight fraction and the mass absorption (attenuation) coefficient, respectively. For a given compound, the weight fraction is defined as follows .

$$w_i = \frac{n_i A_i}{\sum n_j A_j} \tag{3}$$

In this expression, A_i represents the atomic weight of an element, while nin_ini denotes the number of atoms of that element. The total molecular cross section (σ_m) is calculated using the following formulation defined in the literature (Gowda *et al.*, 2005).

$$\sigma_m = \frac{(\mu/\rho)_{C.}}{N_A} M \tag{4}$$

$$M = \sum n_i A_i \tag{5}$$

Here, M denotes the molecular weight, while N_A represents Avogadro's number. The atomic cross section (σ_a) and the electronic cross section (σ_{el}) are calculated using the equations given below (Gowda et al., 2005).

$$\sigma_a = \frac{\sigma_m}{\sum n_i} \tag{6}$$

$$\sigma_e = \frac{1}{N_A} \sum \frac{A_i}{Z_i} f_i \mu_i \tag{7}$$

Here, $f_{i\_}$ denotes the fractional abundance of the element in the compound, while Z_i represents the atomic number of the corresponding constituent element.

$$f_i = \frac{n_i}{\sum n_i} \tag{8}$$

Here, nin_ini represents the number of atoms of the corresponding constituent element. The effective atomic number (Z_{eff}) can be defined as the ratio of the total atomic cross section to the total electronic cross section. In terms of total interactions with photons, the Z_{eff} value can be calculated using the method proposed by Gowda et al. (2005). Additionally, Z_{eff} can also be determined using Equation 10 (Manohara et al., 2008).

$$Z_{eff} = \frac{\sigma_a}{\sigma_b} \tag{9}$$

$$Z_{eff} = \frac{\sum_i f_i A_i \mu_i}{\sum_j f_j \frac{A_j}{Z_j} \mu_j} \tag{10}$$

Here, μ_i represents the total absorption coefficient. Within the framework of Equation (10), the variation in the effective atomic number (Z_{eff}) can be evaluated using the total μ_i coefficients (Gowda et al., 2005).

Additionally, the N_{el} value can be calculated using the method proposed by Manohara (2008).

$$N_{el} = N_A \frac{Z_{eff}}{\langle A \rangle} \tag{11}$$

The average atomic mass is denoted by ⟨A⟩. Parameters such as the half-value layer and the mean free path, which play a crucial role in the interaction of radiation with matter, are directly related to the absorption properties of the material. These quantities can be calculated using the following equations as reported in the relevant studies.

$$HVL = \ln 2 / \mu \tag{12}$$

$$MFP\ (cm) = 1/\mu \tag{13}$$

EABF (Energy Absorption Enhancement Factor) is a parameter that quantitatively expresses the contribution of secondary scattered photons generated by gamma photons passing through a material to the total energy absorbed in the environment. In contrast, the Exposure Buildup Factor (EBF) represents the contribution of scattered photons to the radiation dose in air after passing through the shielding material. These concepts and their differences have been discussed in detail in the literature (Oto et al., 2019). Within this theoretical framework, the EABF and EBF values of the alloys were calculated using the EpiXS software with the Geometric Progression (GP) fitting method, and photon buildup effects were quantitatively evaluated.

RESULTS AND DISCUSSION

In this study, the gamma radiation shielding properties of Cr–Mo–Nb–Ta–V–based high-entropy alloys reinforced with oxide (Ta_2O_5), carbide (HfC), and nitride (TiN) phases were analyzed by presenting the theoretically calculated parameters—obtained using the above-mentioned software programs—in tables and as graphs showing their variation with energy. The results obtained from the calculation programs used in the study showed very good agreement with each other. This consistency of the results supports the reliability and accuracy of the present work. The densities of the constituent elements in the Cr–Mo–Nb–Ta–V-based high-entropy alloys reinforced with oxide (Ta_2O_5), carbide (HfC), and nitride (TiN) phases are listed in Table 1. The mass attenuation coefficients (MAC, cm^2/g) of the investigated composite materials were calculated using the WinXCOM, EpiXS, Phy-X/PSD, and Py-MLBUF software packages. These programs were employed not only to determine the mass attenuation coefficients but also to derive the corresponding photon–matter interaction parameters. The calculated mass attenuation coefficient values are presented in Tables 2 and Table 3.

The mass attenuation coefficient (MAC) is a parameter that indicates how much radiation or light energy a material absorbs per unit mass. In other words, it measures how much radiation is absorbed by each kilogram of the material, independent of its density. This allows materials with different densities to be compared in terms of their energy absorption capabilities. An effective shielding material against gamma radiation is made from a material with a high mass attenuation coefficient; thus, the material absorbs more radiation and acts as a strong radiation-absorbing shield.

Tables 2 and 3 show that the results of the calculations indicate that the mass attenuation coefficient (MAC) values reach their maximum in this energy range, particularly due to the dominance of the photoelectric effect (approximately 0.015-0.15). As is known, the probability of a photoelectric effect occurring is inversely proportional to the energy (E^3) (Monohora, 2008). This indicates that as the energy increases, the photoelectric

dominance decreases. In Figure 1,(according to EpiXS) an increase in MAC values is observed in the 60-80 energy range due to the fact that elements such as Hf and Ta in the alloys have absorption shore energies of approximately 65-67 keV, respectively. As seen in Figure 1, a significant decrease in MAC values is observed as the energy increases. In this study, it is observed that the HfC reinforced composite material has the highest mass attenuation coefficient. At 0.015 keV, the MAC attenuation coefficient of the undoped alloy material was found to be 71.413 cm^2/g, while that of the HfC-doped composite material was 83.691 cm^2/g. This represents a 17.19% increase in radiation shielding efficiency. The second highest was the Ta_2O_5-doped composite material, with a 14.8% increase, resulting in a mass attenuation coefficient of 80.982 cm^2/g. In this study, the TiN-doped material showed the lowest mass attenuation coefficient. This indicates that density is a significant factor in absorption, as the addition of TiN to the pure alloy reduces the density of the composite material. Furthermore, at other energies, the HfC-doped composite material exhibits higher values. In the mid-energy range (0.15-1 MeV), Compton scattering becomes the dominant interaction mechanism, and as photon energy increases, a more gradual decrease in MAC values occurs across all composite materials. At higher photon energies (≥1 MeV), it has been observed that MAC values reach an almost constant level. This indicates that the effect of processes such as pair formation and high-energy scattering increases in the relevant energy range.

The linear attenuation coefficient (LAC), a parameter that indicates how much radiation or light a material absorbs per unit thickness. Its unit is usually cm^{-1} and it is calculated using Equation 1. The larger the coefficient, the more radiation the material absorbs at the same thickness, providing more effective shielding. In other words, materials with a high linear attenuation coefficient better block the passage of radiation.

As shown in Table 4 and Figure 2, the linear attenuation coefficient (LAC) values as a function of photon energy for the materials in the study are graphically presented in Figure 2. In the low energy region (~0.01 MeV), the LAC values are high. As seen here, the results show that a significant decrease in LAC values is observed as the photon energy increases. This indicates that photons pass through the material more easily as the energy

increases. These data provide important information for material characterization and radiation protection applications.

Table 1. *Chemical compositions (wt%) and theoretical density (ρ, g/cm³) values of the Cr–Mo–Nb–Ta–V based high-entropy alloy and oxide/carbide/nitride-reinforced composites (HEA and HEAC1–HEAC3).*

Sample code	wt% Cr	wt % Mo	wt% Nb	wt% Ta	wt% V	wt% Ta_2O_5	wt% HfC	wt% TiN	Theoretical Density (ρ) g/cm³
HEA	10.999	20.296	19.653	38.276	10.776	-	-	-	10.148
HEAC1	8.249	15.222	14.74	28.707	8.082	25	-	-	9.579
HEAC2	8.249	15.222	14.74	28.707	8.082	-	25	-	10.685
HEAC3	8.249	15.222	14.74	28.707	8.082	-	-	25	8.210

Table 2. *Mass attenuation coefficients (MAC, cm²/g) of HEA and HEAC1–HEAC3 high-entropy alloys calculated using different software packages (WinXCOM, EpiXS, Phy-X/PSD, and Py-MLBUF).*

Mass attenuation coefficient ($cm^2.g^{-1}$)												
Photon energy (MeV)	**HEA**				**HEAC1**				**HEAC2**			
	EpiXS	**WinXcom**	**Phy-X/PSD**	**Py-MLBUF**	**EpiXS**	**WinXcom**	**Phy-X/PSD**	**Py-MLBUF**	**EpiXS**	**WinXcom**	**Phy-X/PSD**	**Py-MLBUF**
0.015	71.413	71.66	71.66	71.653	80.982	81.268	81.268	81.258	83.691	83.963	83.964	83.971
0.02	56.173	59.687	59.687	59.687	47.658	57.773	57.773	57.773	48.918	59.031	59.031	59.031
0.03	20.644	20.62	20.62	20.619	19.98	19.961	19.961	19.959	20.402	20.384	20.384	20.383
0.04	9.534	9.536	9.536	9.536	9.254	9.264	9.264	9.262	9.448	9.457	9.457	9.457
0.05	5.225	5.239	5.239	5.239	5.088	5.11	5.11	5.11	5.191	5.215	5.215	5.216
0.06	3.2	3.223	3.223	3.223	3.124	3.156	3.156	3.157	3.183	3.221	3.221	3.221
0.08	3.775	3.767	3.767	3.767	4.395	4.387	4.387	4.386	4.556	4.55	4.55	4.55
0.1	2.141	2.138	2.138	2.138	2.494	2.491	2.491	2.491	2.583	2.579	2.579	2.579
0.15	0.79	0.788	0.788	0.788	0.913	0.911	0.911	0.911	0.941	0.939	0.939	0.939
0.2	0.416	0.415	0.415	0.415	0.474	0.473	0.473	0.473	0.487	0.485	0.485	0.485
0.3	0.198	0.198	0.198	0.198	0.218	0.218	0.218	0.218	0.222	0.222	0.222	0.222
0.4	0.133	0.133	0.133	0.133	0.143	0.143	0.143	0.143	0.144	0.145	0.145	0.145
0.5	0.105	0.105	0.105	0.105	0.11	0.11	0.11	0.11	0.111	0.111	0.111	0.111
0.8	0.071	0.071	0.071	0.071	0.073	0.073	0.073	0.073	0.073	0.073	0.073	0.073
1	0.061	0.061	0.061	0.061	0.062	0.062	0.062	0.062	0.062	0.062	0.062	0.062
1.5	0.048	0.048	0.048	0.048	0.049	0.049	0.049	0.049	0.049	0.049	0.049	0.049
2	0.043	0.043	0.043	0.043	0.043	0.043	0.043	0.043	0.043	0.043	0.043	0.043
3	0.038	0.038	0.038	0.038	0.038	0.038	0.038	0.038	0.038	0.038	0.038	0.038
4	0.036	0.036	0.036	0.036	0.037	0.037	0.037	0.037	0.037	0.037	0.037	0.037
5	0.036	0.036	0.036	0.036	0.036	0.037	0.037	0.037	0.037	0.037	0.037	0.037
6	0.036	0.036	0.036	0.036	0.037	0.037	0.037	0.037	0.037	0.037	0.037	0.037
8	0.037	0.037	0.037	0.037	0.038	0.038	0.038	0.038	0.039	0.039	0.039	0.039
10	0.039	0.039	0.039	0.039	0.04	0.04	0.04	0.04	0.04	0.04	0.04	0.04
15	0.042	0.043	0.043	0.043	0.044	0.044	0.044	0.044	0.045	0.045	0.045	0.045

Table 3. *Mass attenuation coefficients (MAC, cm²/g) of HEAC4 high-entropy alloys obtained from different software programs (WinXCOM, EpiXS, Phy-X/PSD, and Py-MLBUF).*

Mass attenuation coefficient ($cm^2.g^{-1}$)				
Photon energy (MeV)	**HEAC3**			
	EpiXS	**WinXcom**	**Phy-X/ PSD**	**Py-MLBUF**
0.015	60.581	60.754	60.746	60.746
0.02	47.736	47.866	47.865	47.865
0.03	16.465	16.444	16.443	16.443
0.04	7.593	7.593	7.593	7.593
0.05	4.166	4.175	4.175	4.176
0.06	2.559	2.576	2.576	2.576
0.08	2.919	2.913	2.913	2.913
0.1	1.667	1.665	1.665	1.665
0.15	0.632	0.631	0.631	0.631
0.2	0.345	0.344	0.344	0.344
0.3	0.175	0.175	0.175	0.175
0.4	0.123	0.123	0.123	0.123
0.5	0.099	0.099	0.099	0.099
0.6	0.086	0.086	0.086	0.086
1	0.061	0.061	0.061	0.061
1.5	0.048	0.048	0.048	0.048
2	0.043	0.043	0.043	0.043
3	0.037	0.037	0.037	0.037
4	0.035	0.035	0.035	0.035
5	0.034	0.034	0.034	0.034
6	0.034	0.034	0.034	0.034
8	0.034	0.034	0.034	0.034
10	0.035	0.035	0.035	0.035
15	0.038	0.038	0.038	0.038

Figure 1. *Variation of the mass attenuation coefficient (MAC) with photon energy for the high-entropy alloys.*

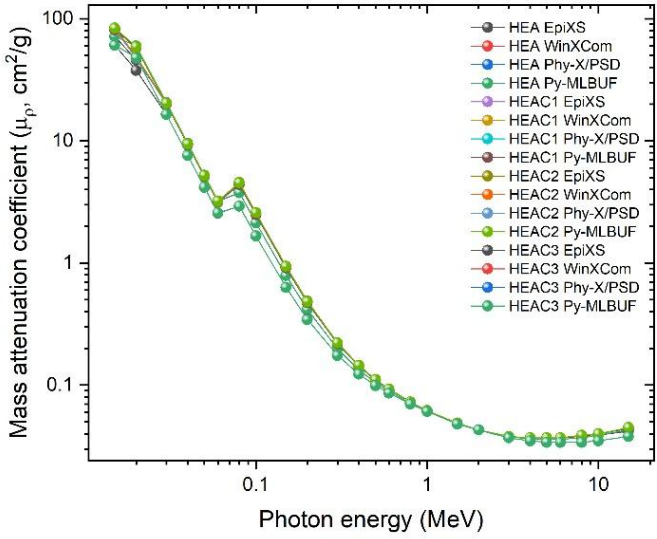

Table 4*. Linear attenuation coefficient (LAC) values of the HEA samples calculated using the EpiXS software.*

Linear Attenuation Coefficient (LAC, cm^{-1})				
Photon energy (MeV)	HEA	HEAC1	HEAC2	HEAC3
0.015	724.683	775.724	894.211	497.384
0.02	468.553	456.516	522.674	309.822
0.03	209.493	191.388	217.984	135.177
0.04	96.747	88.648	100.949	62.339
0.05	53.027	48.739	55.467	34.203
0.06	32.473	29.921	34.013	21.010
0.08	38.309	42.099	48.676	23.967
0.1	21.73	23.894	27.602	13.69
0.15	8.017	8.744	10.059	5.190
0.2	4.226	4.540	5.201	2.831
0.3	2.012	2.089	2.372	1.436
0.4	1.354	1.369	1.544	1.010

0.5	1.063	1.056	1.186	0.816
0.6	0.901	0.883	0.99	0.704
0.8	0.722	0.698	0.779	0.575
1	0.620	0.595	0.663	0.499
1.5	0.490	0.466	0.519	0.397
2	0.432	0.411	0.458	0.349
3	0.384	0.367	0.410	0.305
4	0.368	0.352	0.395	0.288
5	0.364	0.350	0.393	0.281
6	0.366	0.352	0.397	0.279
8	0.377	0.364	0.412	0.283
10	0.392	0.379	0.430	0.291
15	0.431	0.418	0.476	0.314

Figure 2. *Variation of the linear attenuation coefficient (LAC, cm^{-1}) with photon energy for the high-entropy alloys.*

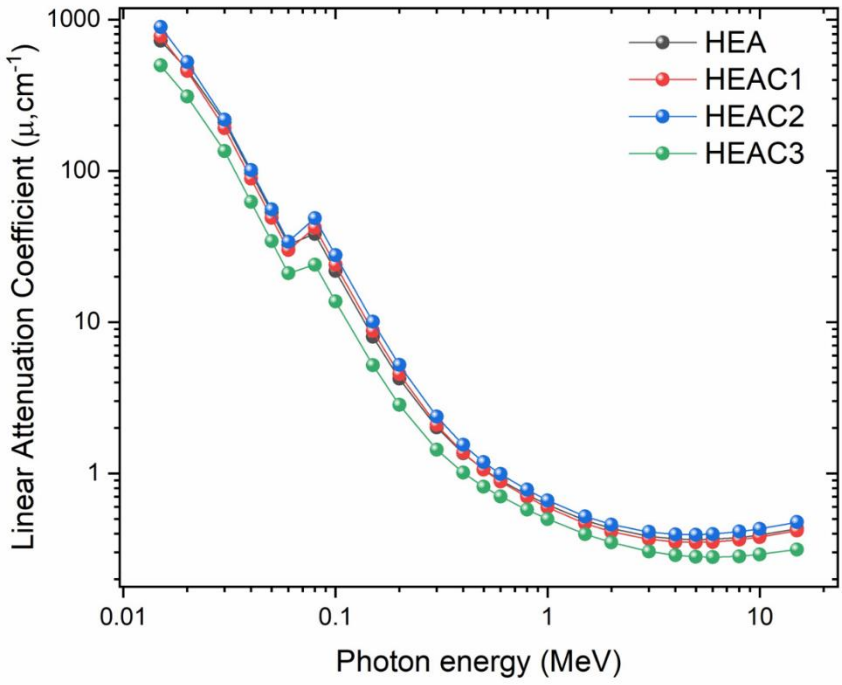

***Table 5**. Mean free path (MFP, cm) values of the HEA samples calculated using the EpiXS software.*

Mean Free Path (cm)				
Photon energy (MeV)	HEA	HEAC1	HEAC2	HEAC3
0.015	0.001	0.001	0.001	0.002
0.02	0.002	0.002	0.002	0.003
0.03	0.005	0.005	0.005	0.007
0.04	0.010	0.011	0.010	0.016
0.05	0.019	0.021	0.018	0.029
0.06	0.031	0.033	0.029	0.048
0.08	0.026	0.024	0.021	0.042
0.1	0.046	0.042	0.036	0.073
0.15	0.125	0.114	0.099	0.193
0.2	0.237	0.220	0.192	0.353
0.3	0.497	0.479	0.422	0.696
0.4	0.739	0.731	0.648	0.990
0.5	0.941	0.947	0.844	1.226
0.6	1.110	1.132	1.010	1.421
0.8	1.385	1.433	1.284	1.739
1	1.612	1.680	1.509	2.002
1.5	2.043	2.144	1.928	2.517
2	2.316	2.431	2.184	2.866
3	2.606	2.727	2.441	3.277
4	2.720	2.838	2.531	3.477
5	2.749	2.861	2.544	3.562
6	2.735	2.842	2.521	3.585
8	2.653	2.749	2.430	3.537
10	2.550	2.638	2.326	3.442
15	2.320	2.392	2.102	3.189

Figure 3. *Variation of the mean free path (MFP) of the HEAs with photon energy.*

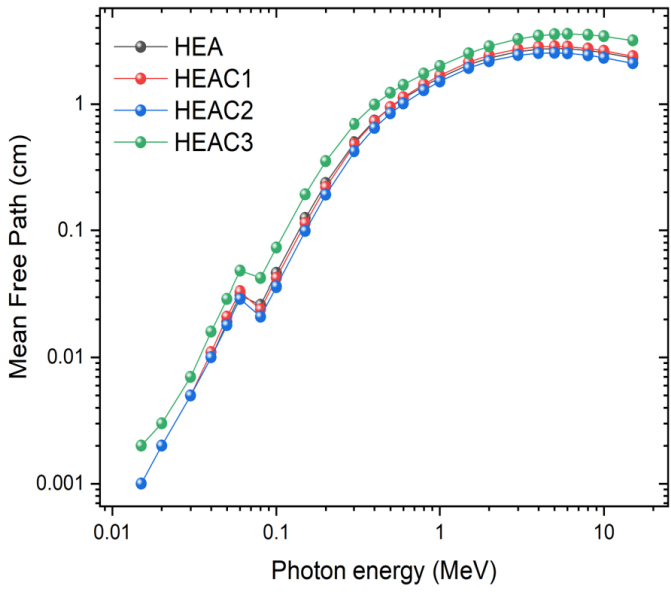

The mean free path (MFP) indicates that radiation is absorbed over a shorter distance within the material, thus exhibiting better shielding performance.As presented in Table 5 and Figure 4, the mean free path (MFP) values of all samples are lower at low photon energies and increase markedly with increasing photon energy. This trend indicates that higher-energy photons are able to travel longer distances within the material. Among the investigated alloys and composites, the HEAC2 sample exhibits the lowest MFP values, confirming its superior radiation shielding performance, whereas the HEAC3 sample demonstrates comparatively the weakest shielding effectiveness.

Table 6. *Half value layer (HVL) values of the HEA samples calculated using the EpiXS software.*

Half Value Layer (HVL, cm)				
Photon energy (MeV)	HEA	HEAC1	HEAC2	HEAC3
0.015	0.001	0.001	0.001	0.001
0.02	0.001	0.002	0.001	0.002
0.03	0.003	0.004	0.003	0.005
0.04	0.007	0.008	0.007	0.011
0.05	0.013	0.014	0.013	0.020
0.06	0.021	0.023	0.02	0.033
0.08	0.018	0.016	0.014	0.029
0.1	0.032	0.029	0.025	0.051
0.15	0.086	0.079	0.069	0.134
0.2	0.164	0.153	0.133	0.245
0.3	0.345	0.332	0.292	0.483
0.4	0.512	0.506	0.449	0.686
0.5	0.652	0.657	0.585	0.850
0.6	0.769	0.785	0.700	0.985
0.8	0.960	0.993	0.890	1.205
1	1.117	1.165	1.046	1.388
1.5	1.416	1.486	1.336	1.745
2	1.605	1.685	1.514	1.987
3	1.806	1.890	1.692	2.272
4	1.885	1.967	1.754	2.410
5	1.905	1.983	1.763	2.469
6	1.896	1.970	1.747	2.485
8	1.839	1.906	1.684	2.452
10	1.768	1.829	1.612	2.386
15	1.608	1.658	1.457	2.210

Figure 4. *Variation of the half value layer (HVL, cm) with photon energy for the high-entropy alloys.*

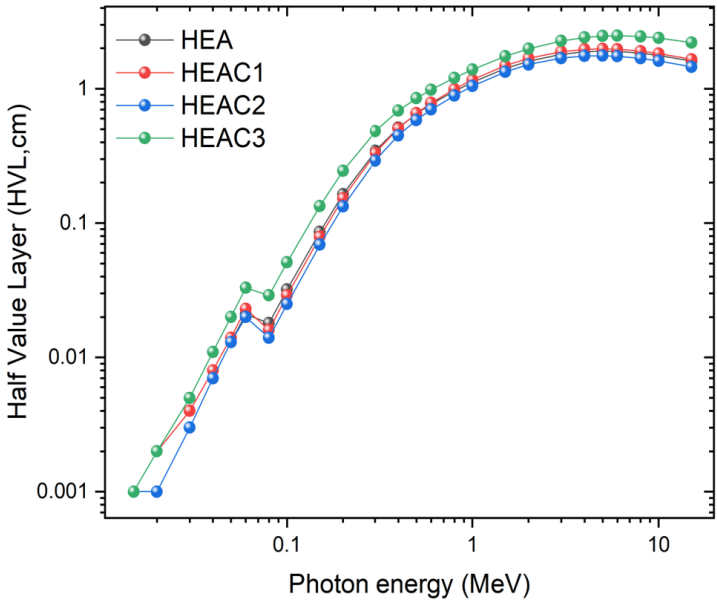

The half-value layer (HVL) is one of the fundamental parameters used to evaluate the radiation shielding effectiveness of a material, where lower HVL values indicate more efficient shielding performance. In particular, reinforced composite materials exhibiting low HVL values provide effective radiation attenuation at smaller thicknesses, offering a significant advantage for radiation shielding applications.

As presented in Table 6 and Figure 4, the half-value layer (HVL) values of all high-entropy alloy and composite materials (HEA, HEAC1, HEAC2, and HEAC3) exhibit a general increasing trend with rising photon energy. This behavior indicates that greater material thicknesses are required to attenuate higher-energy photons. Notably, HEAC3 shows the highest HVL values, implying the need for thicker shielding layers, whereas HEA, HEAC1, and HEAC2 demonstrate

comparatively lower HVL values, reflecting more effective attenuation capability at high photon energies. Among all investigated materials, the HfC-reinforced composite consistently presents the lowest HVL values across the entire energy range, highlighting its superior performance as a radiation shielding material.

Table 7. *Effective atomic number (Z_{eff}) values of the HEA samples calculated using the EpiXS software*

Effective Atomic Number (Z_{eff})				
Photon energy (MeV)	HEA	HEAC1	HEAC2	HEAC3
0.015	52.472	57.612	58.071	44.984
0.02	49.106	53.666	54.07	44.404
0.03	47.526	51.324	51.687	44.249
0.04	47.734	51.436	51.853	44.358
0.05	47.859	51.407	51.909	44.225
0.06	47.881	51.209	51.824	43.855
0.08	60.324	63.511	63.919	56.321
0.1	60.02	62.817	63.478	54.861
0.15	57.971	59.686	61.167	49.517
0.2	55.204	55.794	58.11	44.142
0.3	50.271	49.04	52.449	36.918
0.4	47.118	44.764	48.643	33.306
0.5	45.252	42.234	46.311	31.431
0.6	44.096	40.67	44.842	30.357
0.8	42.85	38.979	43.209	29.259
1	42.22	38.126	42.38	28.729
1.5	41.708	37.46	41.715	28.339
2	41.834	37.73	41.95	28.545
3	42.444	38.864	42.963	29.374
4	43.068	40.053	44.005	30.274
5	43.6	41.1	44.905	31.099
6	44.033	41.984	45.65	31.819
8	44.69	43.365	46.791	32.993
10	45.159	44.373	47.609	33.886
15	45.912	45.985	48.899	35.366

Figure 5. *Variation of the effective atomic number (Z_{eff}) with photon energy for the high-entropy alloys.*

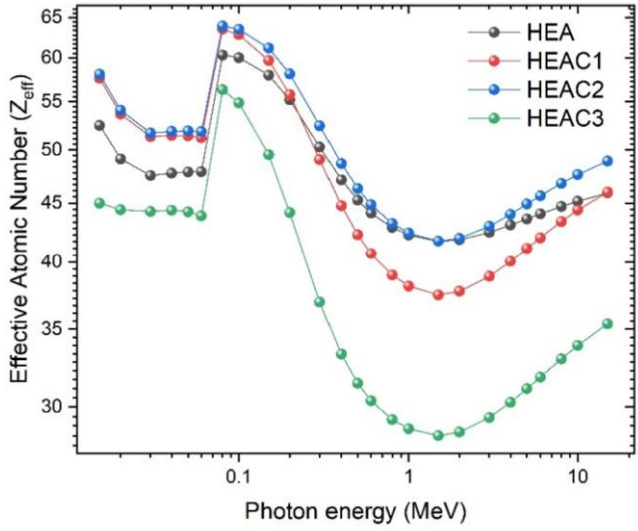

The effective atomic number (Z_{eff}) is a conceptual parameter used particularly in radiation–matter interactions, which represents the photon interaction behavior of a compound, alloy, or composite material by a single equivalent atomic number. In this study, Table 7 and Figure 5 examine the effective atomic number (Z_{eff}) values of HEA, HEAC1, HEAC2, and HEAC3 samples as a function of photon energy. The highest Zeff values are observed in the low energy range (0.015-0.2 MeV). The increases in the energy range between 0.07 MeV and 0.2 MeV are due to the high atomic number elements in the materials, as their K absorption shore energy ranges are located in this region. In the mid-energy range (0.1–1.5 MeV), a decrease in MAC values is observed as Compton scattering becomes dominant, while Z_{eff} values approach a minimum. This indicates that the effect of atomic structure on attenuation is reduced, and all samples exhibit

similar performance. In the high-energy regions (>1 MeV), Z_{eff} tends to increase again. In this energy range, the shielding efficiency of the material remains at moderate levels due to the activation of the pair formation mechanism. Overall, the HEAC3 sample exhibits lower performance in terms of both MAC and Z_{eff}. Furthermore, the study shows that HfC-doped high-entropy alloy provides more effective photon shielding in the low and medium energy range.

Table 8. *Electron density (Nel, electrons·g^{-1}) values of the HEA samples calculated using the EpiXS software.*

Electron Density (Nel, elektron·g^{-1})				
Photon energy (MeV)	HEA	HEAC1	HEAC2	HEAC3
0.015	3.342	4.126	3.692	4.338
0.02	3.128	3.844	3.438	4.282
0.03	3.027	3.676	3.286	4.267
0.04	3.04	3.684	3.297	4.278
0.05	3.048	3.682	3.3	4.265
0.06	3.05	3.668	3.295	4.229
0.08	3.842	4.549	4.064	5.431
0.1	3.823	4.499	4.036	5.29
0.15	3.692	4.275	3.889	4.775
0.2	3.516	3.996	3.694	4.257
0.3	3.202	3.512	3.335	3.56
0.4	3.001	3.206	3.093	3.212
0.5	2.882	3.025	2.944	3.031
0.6	2.809	2.913	2.851	2.927
0.8	2.729	2.792	2.747	2.822
1	2.689	2.731	2.694	2.771
1.5	2.657	2.683	2.652	2.733
2	2.665	2.702	2.667	2.753
3	2.703	2.783	2.731	2.833
4	2.743	2.869	2.798	2.919
5	2.777	2.944	2.855	2.999
6	2.805	3.007	2.902	3.068
8	2.846	3.106	2.975	3.182
10	2.876	3.178	3.027	3.268
15	2.924	3.293	3.109	3.411

Figure 6. *Variation of the electron density (Nel) of the HEAs with photon energy.*

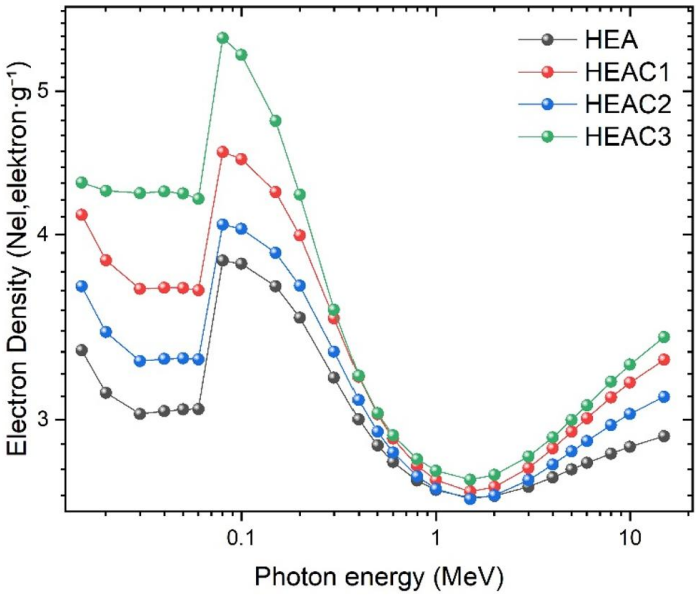

The electron density (N_{el}) refers to the total number of electrons per unit mass or volume of a material and is one of the fundamental parameters governing the probability of photon matter interactions. An increase in electron density indicates an enhancement in radiation shielding effectiveness, particularly in energy regions where Compton scattering is the dominant interaction mechanism**.** An examination of the data presented in Table 8 and Figure 6 reveals that the variation of electron density with photon energy closely follows the trend observed for the effective atomic number (Z_{eff}). The N_{el} values attain their maximum levels in the low-energy region (0.015-0.2 MeV), where photoelectric absorption is predominant. With increasing photon energy, a pronounced decrease in electron density is observed, reaching minimum values around 1 MeV. This behavior is attributed to the dominance of Compton scattering in this energy

range, which reduces the probability of photon–matter interactions. At higher photon energies (≥ 1 MeV), a gradual increase in N_{el} values is detected due to the growing contribution of the pair production mechanism. Among the investigated samples, the HEAC3 specimen exhibits the highest electron density over the entire energy range, which can be attributed to its lower average atomic mass, leading to a higher number of electrons per unit mass. In general, an increase in electron density enhances the likelihood of photon interactions, thereby indicating an improvement in the radiation shielding effectiveness of the material.

Figure 7. *Variation of the energy absorption buildup factors (EABF) with photon energy at different penetration depths (1–15 mfp) for the high-entropy alloy (HEA) samples.*

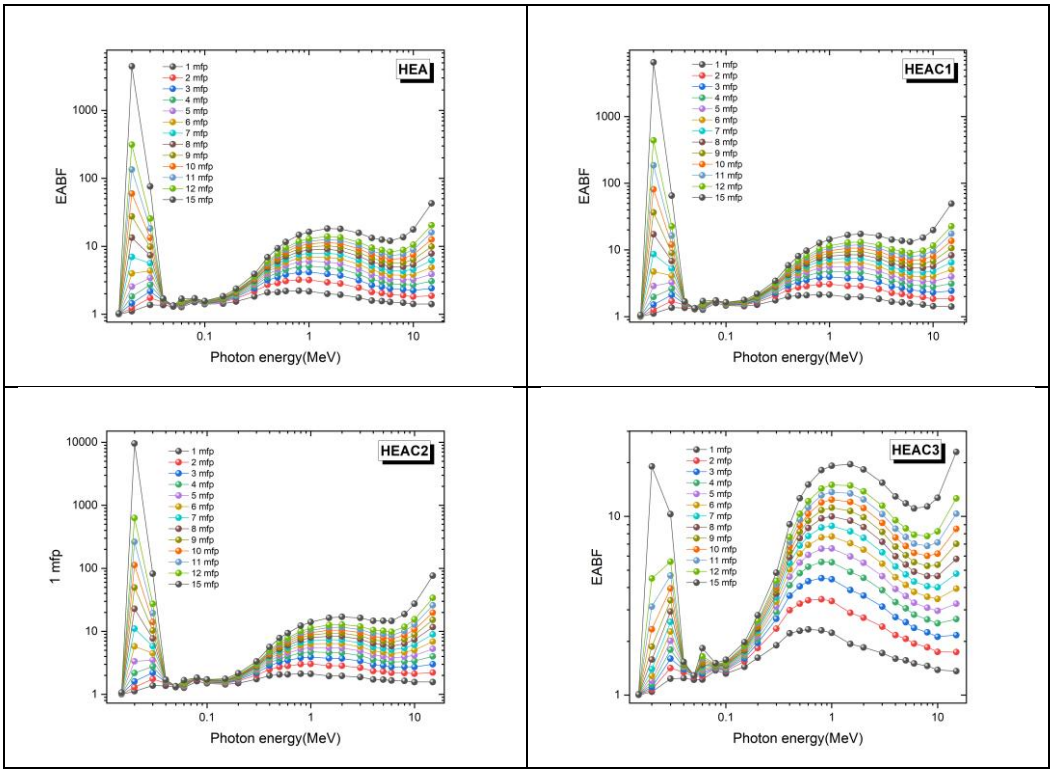

The Energy Absorption Buildup Factor (EABF) is a parameter that quantifies the contribution of secondary photons generated by scattering processes within a shielding material to the total absorbed energy. As the EABF value increases, the effect of multiple scattering inside the material becomes more pronounced; therefore, higher EABF values indicate lower energy absorption efficiency, whereas lower EABF values correspond to improved radiation shielding performance.

In Figure 7, the Energy Absorption Deposition Factor (EABF) values for all samples start at low levels at low photon energies and increase significantly as the energy increases, forming a distinct peak in the mid-energy region. This peak corresponds to the energy range where multiple scattering and absorption processes within the material are most intense. As the photon energy continues to increase, the EABF values decrease again and show a more stable trend at higher energy levels. At all energies, HEA, HEAC1, and HEAC2 have lower EABF values compared to other HEAC materials, indicating good radiation shielding performance.

Figure 8. *Variation of the exposure buildup factors (EBF) with photon energy at different penetration depths (1–15 mfp) for the high-entropy alloy (HEA) samples.*

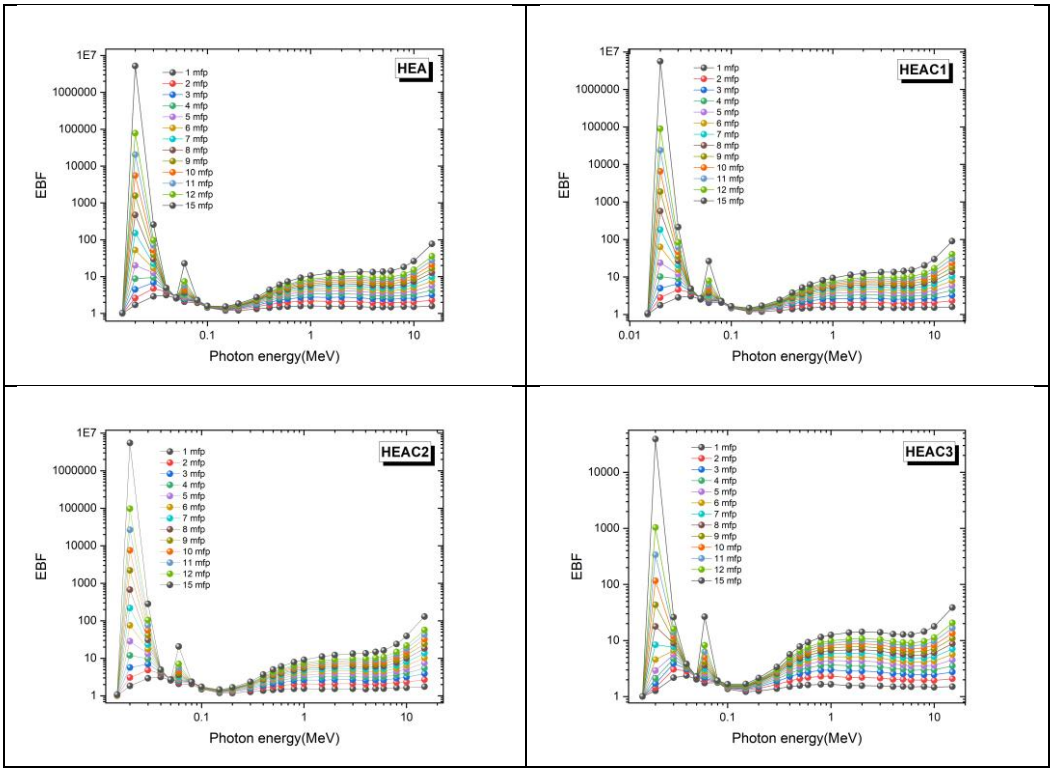

The Exposure Buildup Factor (EBF) is a parameter that represents the contribution of secondary radiation generated by photon scattering within a shielding material to the total radiation exposure. Higher EBF values indicate increased exposure due to multiple scattering events and, consequently, reduced shielding effectiveness, whereas lower EBF values signify more effective radiation shielding performance. As shown in Figure 8, the significant increases and local fluctuations observed in the Exposure Deposition Factor (EBF) values in the low to medium energy range for all samples are due to the high

atomic number elements present in the alloy compositions. These are particularly attributed to the strong interactions near the absorption edges with high atomic number elements Hf and Ta.

CONCLUSION

The mass attenuation coefficient (MAC) and effective atomic number (Z_{eff}) values obtained from the WinXCOM, EpiXS, and Phy-X/PSD software packages exhibit mutually consistent results within the numerical uncertainty limits of theoretical models across the entire energy range. For all investigated samples (HEA, HEAC1, HEAC2, and HEAC3), high MAC and Z_{eff} values were observed in the low-energy region, indicating that the materials effectively absorb photons in energy ranges where the photoelectric effect is dominant. In the intermediate energy region, as Compton scattering becomes the prevailing interaction mechanism, a noticeable decrease in both MAC and Z_{eff} values was recorded. At higher photon energies, Z_{eff} values exhibit a tendency to increase again, whereas MAC values remain approximately constant.

Comparative analyses reveal a high degree of agreement among the predictions of the four computational tools, thereby confirming the reliability of the theoretical estimations. The results further demonstrate that the HEAC2 sample (hafnium-reinforced high-entropy alloy) exhibits superior performance for photon shielding applications over a broad energy range. HEAC2 stands out among the investigated alloys by exhibiting higher MAC and Z_{eff} values, along with lower half-value layer (HVL), energy absorption buildup factor (EABF), and exposure buildup factor (EBF) values. These findings highlight that incorporating heavy, high–atomic-number elements into alloy compositions represents a critical design strategy for enhancing photon shielding performance and provides an important pathway for the development of advanced radiation shielding materials.

REFERENCES

A.S. Abouhaswa, S. Kalecik, E. Kavaz, Newly designed borate glass system for optical and radiation shielding applications: multiple effects of CdS on structural, magnetic, optical, mechanical and photon shielding features, Ceram. Int. 48 (2022) 27120–27129, https://doi.org/10.1016/j.ceramint.2022.06.023.

Adamson, R. B., Coleman, C. E., & Griffiths, M. (2019). Irradiation creep and growth of zirconium alloys: A critical review. *Journal of Nuclear Materials*, *521*, 167-244.

Alım, B. (2020). A comprehensive study on radiation shielding characteristics of Tin-Silver, Manganin-R, Hastelloy-B, Hastelloy-X and Dilver-P alloys. *Applied Physics A, 126*(4), 262.

Gerward, L.; Guilbert, N.; Jensen, K. B.; Levring, H. 2004, WinXCom – a program for calculating X-ray attenuation coefficients. Radiat. Phys. Chem. 71(3–4), 653–654.

Gowda, S., Krishnaveni, S., & Gowda, R. (2005). Studies on effective atomic numbers and electron densities in amino acids and sugars in the energy range 30–1333 keV. *Nuclear Instruments and Methods in Physics Research Section B: Beam Interactions with Materials and Atoms*, *239*(4), 361-369.

Hila F.C., Asuncion-Astronomo A., Dingle C.A.M., Jecong, J.F.M., Javier- Hila A.M.V., Gili M.B.Z., Balderas C.V., Lopez G.E.P., Guillermo N.R.D., Amorsolo A.V., 2021. EpiXS: a Windows-based program for photon attenuation, dosimetry and shielding based on EPICS2017 (ENDF/B-VIII) and EPDL97 (ENDF/B-VI.8), Radiat. Phys. Chem. 182, 109331

Kavgacı, M., Yaykas¸lı, H., Eskalen, H., Peris¸ano˘glu, U., Yılmaz, R., Tunç, H., Peris¸ano˘ glu, E.K., 2024. Analysis of structural, optical, mechanical properties and evaluation of radiation shielding effectiveness of strontium borate glasses doped with ZnO nanoparticles. *Ceram. Int. 50*, 25256–25272. https://doi.org/10.1016/j. ceramint.2024.04.256.

Mann K.S., Mann J.S., Py-MLBUF: A Python-based web application for multilayer photon shielding calculations. *Radiation Physics and Chemistry* 194, 110056 (2022).

Madak, Z., Oto, B., Kavaz, E., & Çakar, N. (2025). The gamma and neutron shielding performance of CeO2 and Er2O3 doped Al2Si2O5 (OH) 4–KAlSi3O8–SiO2 ceramics. *Applied Radiation and Isotopes*, 112258.

Mariyappan, M., Marimuthu, K., Sayyed, M. I., Dong, M. G., & Kara, U. (2018). Effect Bi2O3 on the physical, structural and radiation shielding properties of Er3+ ions doped bismuth sodiumfluoroborate glasses. *Journal of Non-Crystalline Solids*, *499*, 75-85.

Manohara, S. R., Hanagodimath, S. M., Thind, K. S., & Gerward, L. (2008). On the effective atomic number and electron density: a comprehensive set of formulas for all types of materials and energies above 1 keV. *Nuclear Instruments and Methods in Physics Research Section B: Beam Interactions with Materials and Atoms*, *266*(18), 3906-3912.

Onaizi, A. M., Amran, M., Tang, W., Betoush, N., Alhassan, M., Rashid, R. S., ... & Onaizi, S. A. (2024). Radiation-shielding concrete: A review of materials, performance, and the impact of radiation on concrete properties. *Journal of Building Engineering*, *97*, 110800.

Oto B., Erden Gülebağlan S., Madak Z., Kavaz E .2019."Effective Atomic Numbers, Electron Densities and Gamma Rays Buildup Factors of Inorganic Metal Halide Cubic Perovskites $CsBX_3$ (B = Sn, Ge; X = I, Br, Cl)." Radiation Physics and Chemistry,vol.159,pp.195-206.

Rasul, S.Y., Aktas, B., Yilmaz, D., Pathman, A.F., Yalcin, S., Acikgoz, A., 2025. Impact of HfO2 on the structural, thermal, gamma, and neutron shielding properties of boro- tellurite glasses. *Inorg. Chem. Commun. 174,* 113993. https://doi.org/10.1016/j. inoche.2025.113993.

Sakar, E.; Özpolat, O. F.; Alım, B.; Sayyed, M. I.; Kurudirek, M. 2020, Phy-X / PSD: Development of a user friendly online software for calculation of parameters relevant to radiation shielding and dosimetry. Radiat. Phys. Chem. 166, 1–12.

Saudi, H.A., Gomaa, H.M., 2019. The effect of Nb2O5 on fast neutron removal cross section, optical, and structural properties of some calcium borate oxide glasses containing Bi3+ ions. *Radiat. Detect. Technol. Methods* 3, 7. https://doi.org/ 10.1007/s41605-018-0083-x.

Şakar, E. (2020). Determination of photon-shielding features and build-up factors of nickel–silver alloys. *Radiation Physics and Chemistry*, *172*, 108778.

Yalcin, S., Aktas, B., Yilmaz, D., 2019. Radiation shielding properties of Cerium oxide and Erbium oxide doped obsidian glass. *Radiat. Phys Chem*.160,83–88.https:// doi.org/10.1016/j.radphyschem.2019.03.024.

Zorla, E., Ipbüker, C., Biland, A., Kiisk, M., Kovaljov, S., Tkaczyk, A. H., & Gulik, V. (2017). Radiation shielding properties of high performance concrete reinforced with basalt fibers infused with natural and enriched boron. *Nuclear engineering and Design*, *313*, 306-318.

Wang, K., Hu, J., Chen, T., Zhang, W., Fan, H., Feng, Y., ... & Wang, K. (2021). Flexible low-melting point radiation shielding materials: soft elastomers with GaInSnPbBi high-entropy alloy inclusions. *Macromolecular Materials and Engineering*, *306*(12), 2100457.

.


BİDGE